Chemical Engineering Journal 512 (2025) 162456

Contents lists available at ScienceDirect

Chemical Engineering Journal

journal homepage: www.elsevier.com/locate/cej

Hierarchical porous one-dimensional N-doped C framework comprising ultrafine Mo_2C catalysts for stable Na/K–Se batteries: Experimental and theoretical investigations☆

Sung Woo Cho [a,1], Hyun Ho Choi [a,1], Thillai Govindaraja Senthamaraikannan [b], Dong–Hee Lim [b], Gi Dae Park [c], Chungyeon Cho [d], Sang Mun Jeong [e], Rakesh Saroha [a,f,*], Jung Sang Cho [a,g,h,*]

[a] Department of Engineering Chemistry, Chungbuk National University, Cheongju 361-763, Republic of Korea
[b] Department of Environmental Engineering, Chungbuk National University, Cheongju 361-763, Republic of Korea
[c] Department of Advanced Materials Engineering, Chungbuk National University, Cheongju 361-763, Republic of Korea
[d] Department of Carbon Convergence Engineering, College of Engineering, Wonkwang University, Iksan 54538, Republic of Korea
[e] Department of Chemical Engineering, Chungbuk National University, Cheongju 361-763, Republic of Korea
[f] Department of Materials Science and Engineering, Ajou University, 206 Worldcup-ro, Yeongtong-gu, Suwon-si, Gyeonggi-do 16499, Republic of Korea
[g] Biomedical Research Institute, Chungbuk National University Hospital, Cheongju 361-763, Republic of Korea
[h] Advanced Energy Research Institute, Chungbuk National University, Cheongju 361-763, Republic of Korea

ARTICLE INFO

Keywords:
Porous carbon frameworks
N-doping
Metal carbide catalyst
Metal–selenium batteries
Full cells

ABSTRACT

This study explores the integration of a highly porous and conductive N-doped carbonaceous framework (P–N–C) with ultrafine molybdenum carbide (Mo_2C) catalysts and utilized it as an outstanding cathode host for Se infiltration (Se@P–N–C@Mo_2C). The one-dimensional (1D) porous structure is obtained by typical electrospinning, followed by carbonization. The complete thermal decomposition of the elongated polystyrene phase generates 1D continuous macroporous tunnel-like channels, and subsequent potassium hydroxide (KOH) activation induces micropore formation. The macroporous channels facilitate easy electrolyte percolation, ensuring smooth and rapid electron/ion diffusion by decreasing the diffusion length and accommodating undesirable volume perturbations. The KOH-induced micropores enable the efficient infiltration of high Se amounts. Additionally, N-doping in the carbon species enhances the electronic conductivity of the nanostructure. The ultrafine Mo_2C catalysts facilitate the efficient trapping and electrocatalytic conversion of Na/K–polyselenide species *via* an electrophilic coupling interaction between $Mo^{\delta+}$ and Se_x^{2-} in Mo_2C and Na_2Se_x or K_2Se_x species, respectively, thereby enhancing active-material utilization. Consequently, the cell comprising the Se@P–N–C@Mo_2C cathode exhibits high-rate capability (up to 10.0C) and long-term cycling stability at 0.5C and 1.0C (400 cycles each), when tested for Na-ion storage. Similarly, a high and stable discharge capacity, 235 mA h g^{-1} (87 % retention, 220 cycles), is observed at a C-rate of 1.0C in K-ion storage. As an anode in full-cell configuration, the Se@P–N–C@Mo_2C electrode achieves reversible Na/K-ions insertion/de-insertion, highlighting its suitability for commercial applications.

1. Introduction

Lithium–sulfur (Li–S) batteries are considered suitable alternatives to the existing Li-ion batteries mostly because of their high theoretical discharge capacity (1675 mA h g^{-1}), high gravimetric (2600 Wh Kg^{-1}) and volumetric (2800 Wh L^{-1}) energy densities, inexpensiveness owing to S abundance, and considerable discharge potential (~2.1 V) *vs.* Li/Li^+ [1–4]. However, the parasitic electrochemical reactions between S and it's discharge product (i.e., Li_2S) cause severe cell issues, such as high active-material loss, poor Coulombic efficiency (CE), safety issues, and inferior cycling performance [5–8]. Selenium (Se), which is in the same group as S on the periodic table, represents a potential alternative owing

☆ This article is part of a special issue entitled: 'Electrochemical Energy' published in Chemical Engineering Journal.

* Corresponding authors at: Department of Engineering Chemistry, Chungbuk National University, Cheongju 361-763, Republic of Korea.
E-mail addresses: rakeshsaroha.18787@gmail.com (R. Saroha), jscho@cbnu.ac.kr (J.S. Cho).

[1] These authors contributed equally to the work.

https://doi.org/10.1016/j.cej.2025.162456

Available online 8 April 2025

to its similar electrochemical properties to those of S. Moreover, Se exhibits numerous other advantages over S, such as considerable theoretical discharge capacity (675 mA h g^{-1}), comparable volumetric capacity (3253 mA h cm^{-3}), high electrical conductivity (~10^{-2} S m^{-1}), and low side reactions attributed to its lower reactivity than S [9–11]. However, similar to their S-based counterparts, Se-based batteries also suffer from Li polyselenide (LiPSe) diffusion in the charge–discharge process [12]. Consequently, numerous studies have focused on enhancing the rate and cycling performance of the Li–Se battery system using advanced cathode hosts, such as microporous carbon [13], three-dimensional (3D) mesoporous carbon/graphene carbon [14], hollow carbon microspheres [15], N-doped carbon aerogels [16], heteroatom-doped microporous carbon [17], porous carbon microcubes [18], and graphitized porous carbon [19].

Similar to Li, sodium (Na) and potassium (K)-based Se (Na–Se and K–Se) batteries are attracting considerable attention mainly because of the similar conversion reactions involving Se as an active cathode [19,20]. Additionally, the natural abundance of Na and K precursors compared with Li decreases the effective cost of the cell [21–23]. However, bulk Se particles cannot be directly applied to Na/K–Se batteries because of the low active-material utilization and poor electrochemical performance. Moreover, the rapid capacity fading of Na/K–Se batteries is mainly attributed to the large ionic radii of Na and K, which cause slight sluggish diffusion kinetics, volume variation of Se, and the shuttle effect of high-order Na– and K–polyselenides (PSes) during the charge/discharge process [24]. Correspondingly, numerous carbon composite cathodes have been investigated as hosts for the Na/K–Se system similar to Li–Se [19,25–32]. However, most of the composites utilize carbon hosts which are sp^2-hybridized graphitic carbon and exhibits graphenic nanodomains that contribute high electronic conductivity [19]. Moreover, the complete confinement of PSes cannot be achieved because of the nonpolar nature of carbon. Further, most graphitized carbon hosts lack sufficient porosity to buffer volume breath and facilitate electrolyte infiltration [33]. Overall, poor interaction between the nonpolar carbon host and polar PSe molecules causes active-material loss, resulting in inferior electrochemical performance. Notably, only a few reports to date have utilized electrocatalysts to efficiently convert PSe species. For instance, Cakan et al., investigated cubic Mn_2O_3 as an electrocatalyst for the Na–Se system, demonstrating superior rate capabilities [34]. Likewise, Manthiram et al., reported N-doped Fe_3C as an efficient polyselenide reservoir for high-performance Na–Se batteries [35]. These studies highlight the effectiveness of electrocatalysts in improving battery performance. However, most previous reports have focused on carbon-selenium composites, indicating significant room for further research and development in this area of electrocatalysts for converting PSes.

Here, we investigate a unique one-dimensional (1D) nanofiber (NF) architecture with a hierarchical porous structure. This architecture comprises polystyrene (PS)–derived continuous longitudinal tunnel-like channels and well-implanted ultrafine molybdenum carbide (Mo_2C) catalysts within an N-doped carbon (N–C) framework (P–N–C@Mo_2C NFs). This porous and highly conductive host was employed as a robust Se host (Se@P–N–C@Mo_2C NFs) to enhance the high-rate and long cycling performances of Na/K-ion batteries. The porosity of the 1D polyacrylonitrile (PAN)-derived carbon NFs involves *in-situ* and *ex-situ* processes. In the *in-situ* process, i.e., carbonization, the electric field–induced island-shaped PS phase (formed during electrospinning) decomposed into hollow macropore-type continuous channels, whereas the potassium hydroxide (KOH)-derived micropores were introduced into the nanostructure in the *ex-situ* process. This bimodal strategy contributes to the overall enhancement of electrochemical properties through several means, including: (1) ensuring efficient electrolyte penetration along with effective volume accommodation owing to the presence of porous channels, (2) high active-material infiltration mainly governed by the micropores, (3) robust electrode integrity by mitigating the pulverization effect, and (4) facilitating the confinement of PSe species within the micropores, thus inhibiting the shuttling process. Furthermore, the ultrafine Mo_2C catalysts, which are formed during KOH activation, are also used as active chemisorption sites. Notably, Mo_2C exhibits high electronic conductivity, reaching ~10^2 S cm^{-1} [36]. This property plays a pivotal role in supporting rapid charge transfer in electrocatalytic conversion processes. Moreover, the availability of various Mo valence states, such as Mo^{4+} and Mo^{6+}, further facilitates the conversion rates of Na/K–PSes by enhancing electrophilic interactions [37]. The capability of ultrafine Mo_2C catalysts to accelerate electrocatalytic conversion is instrumental to mitigating PSe diffusion toward the anode, thereby improving active-material utilization during prolonged cycling. Furthermore, N-doping in the PAN-derived carbon framework primarily enhances the overall electronic conductivity of the nanostructure due to high electronegativity of N compared with C, and this benefits the realization of faster redox kinetics [38]. The synergy between the hierarchical porous, highly conductive, and polar material guarantees structural robustness, which eventually benefits the realization of superior rate and cycling performances. To the best of our knowledge, no reports available in the literature for analyzing the electroctalytic performance of Mo_2C species in highly reversible Na/K–Se battery systems.

Based on the aforementioned structural advantages, the Se-infiltrated sample, denoted as Se@P–N–C@Mo_2C NFs, demonstrates exceptional high-rate performance (up to 10.0C) and prolonged cycling stability and longevity, withstanding 400 cycles at 0.5 and 1.0C-rates, when applied to Na-ion batteries. Similarly, as a K-ion cathode, Se@P–N–C@Mo_2C NFs demonstrate considerable rate capability (up to 2.0C) and satisfactory cycling performance (78 % and 87 % retention at 0.1 and 1.0C, respectively). Even in a full-cell configuration, the electrode demonstrates reversible Na/K-ion intercalation/deintercalation, underscoring its suitability for commercial applications. These advancements (regarding the structural design and electrochemical performance) significantly enhance our understanding of advanced nanostructures and their wide application range.

2. Experimental section

2.1. Materials synthesis

One-dimensional P–N–C@Mo_2C NFs were prepared *via* a multistep process involving conventional electrospinning, carbonization, and KOH activation. Briefly, 0.24 M bis(acetylacetonato)dioxomolybdenum (VI), $(C_5H_7O_2)_2MoO_2$ (Thermo Fisher Scientific; >97 %, Mw = 326.15), was first dispersed in 25 mL of N,N-dimethylformamide (DMF, Samchun Chemicals, 99.5 %) with continuous stirring. Subsequently, 1.0 g of PS (Sigma-Aldrich, Mw = 192,000) was added to the solution. Finally, 2.0 g of PAN (Sigma-Aldrich, Mw = 150,000) was added to this solution as the carbon source and stirred overnight to ensure the homogeneous dispersion of the constituent species. Thereafter, the colloidal solution was loaded into a plastic syringe pump (12 mL) fitted with a 21-gauge stainless-steel needle and ejected at a speed of 1.0 mL h^{-1}. The as-spun fibers were collected onto a rotating drum (180 rpm) covered with Al foil, which was set at a distance of 18 cm from the tip of the needle. The applied voltage between the collector and needle was fixed at 20 kV. Next, the as-spun composite fibers were stabilized in the air for 12 h at 150 °C, after which they were carbonized at 800 °C for 5 h at a heating rate of 5 °C min^{-1} under a N_2 atmosphere. Afterward, the carbonized fibers were mixed with KOH (Samchun Co.) in a 1:2 mass ratio using pestle/mortar, followed by heat-treatment-induced activation for 1 h at 800 °C and a ramp rate of 5 °C min^{-1} in an N_2 atmosphere. Next, the fibers were washed several times with distilled water, after which they were dried. Hereafter, the product is denoted P–N–C@Mo_2C NFs. Thereafter, the obtained powders were physically mixed with elemental Se (Sigma-Aldrich, 99.99 %) in a 1:2 mass ratio and subjected to a two-stage selenization process in an N_2 atmosphere at a heating rate of 5 °C min^{-1}. In the initial step, which was performed at 260 °C for 12 h,

Se impregnation proceeded within the micropores of the nanostructure, whereas the heat treatment at 350 °C for 1 h facilitated the removal of the Se species on the surface. Furthermore, a sample without Mo-salt was prepared by a similar process, as aforementioned, followed by Se infiltration. This sample was denoted as Se@P–N–C NFs.

2.2. Synthesis of $Na_3V_2(PO_4)_3$/carbon (NVP/C) composite

The $Na_3V_2(PO_4)_3$/carbon (NVP/C) composite was prepared using a spray drying process, with post-treatment under an H_2/Ar atmosphere. The spray solution was prepared by dissolving sodium carbonate monohydrate ($Na_2CO_3{\cdot}H_2O$, Samchun), ammonium vanadate (NH_4VO_3, Samchun), and ammonium dihydrogen phosphate ($NH_4H_2PO_4$, Junsei) in a molar ratio of 3:4:6, in water. 15 % excess sodium carbonate monohydrate was added to compensate for salt evaporation. The total molar concentration of the solution was 0.15 mol dm^{-3}. Dextrin ($(C_6H_{10}O_5)_n$, Samchun) was added to the solution (15 g dm^{-3}). A two-fluid nozzle was used as an atomizer, at a pressure of 2.4 bar. The temperatures of the inlet and outlet of the spary dryer were fixed at 300 °C and 110 °C, respectively. The spary-dried powders were post-treated at 800 °C for 5 h under 10 % H_2/Ar gas atmosphere.

2.3. Characterization techniques

The crystal structure of the synthesized nanofibers was determined using a Bruker X-ray diffraction instrument (D2, 2nd generation) equipped with Cu Kα radiation (λ = 1.5418 Å). Morphological analyses were conducted using field-emission scanning electron microscopy (FE–SEM, Zeiss) and field-emission transmission electron microscopy (FE–TEM) (JEM-2100F; JEOL) at the Korea Basic Science Institute (Daegu). High-Angle Annular Dark-Filed Scanning Transmission Electron Microscopy (HAADF–STEM) imaging technique was used to obtain further morphological characteristics of ultrafine Mo_2C nanocrystals. Thermogravimetric analysis (TGA) was performed in an air atmosphere from 25 to 800 °C at a ramp rate of 10 °C min^{-1}. The bonding states and chemical environments of the different elements within the prepared powders were determined using X-ray photoelectron spectroscopy (XPS) (K-Alpha; Thermo Scientific) with an Al Kα X-ray source. The specific surface area and pore size distribution of the synthesized powders were determined using N_2 adsorption–desorption isotherms, with calculations based on the Brunauer–Emmett–Teller (BET) method. Elemental analysis (EA) was employed to quantify the carbon and nitrogen content of the samples. The crystalline characteristics of the carbonaceous products in the prepared microspheres were studied using Raman spectroscopy (LabRam, HR800, Horiba Jobin-Yvon).

2.4. Electrochemical measurements

The electrochemical properties of the samples were measured using 2032-type coin cells. The working electrodes composed of active material, conductive carbon (Super-P), and sodium carboxymethyl cellulose as a binder in a mass ratio of 8:1:1 was prepared using a slurry casting method on an Al foil, which were subsequently dried overnight at 60 °C in a hot air oven. The circular electrodes (ϕ = 14 mm) with a mass loading of ~1.0 mg cm^{-2} (active material mass = 0.72 mg) were punched and transferred inside the glovebox. The Na/K metal and Whatman glass fiber (GF) were used as the counter electrode and separator, respectively. The electrolyte used was 1.0 M $NaClO_4$ in a mixture of ethylene carbonate (EC) and diethyl carbonate (DEC) with a volume ratio of 1:1. For K–ion storage investigations, 0.7 M KPF_6 in EC: DEC was used as electrolyte. The electrochemical performances of the samples were evaluated using CV, charge–discharge testing, and EIS. The voltage window throughout the electrochemical tests was fixed at 0.5–3.0 V. The CV measurements of the samples were performed at various scan rates ranging from 0.1–1.0 mV s^{-1}. The charge–discharge testing of the samples was conducted at various current rates from 0.1 to 10.0C for Na–Se cells and 0.1 to 2.0C for K–Se cells. The C–rate was determined by equating 1C to 675 mA h g^{-1}. Galvanostatic Intermittent Titration Technique (GITT) was performed by applying a current pulse at 0.1C-rate for 10 min followed by relaxation for 1 h. The EIS data of the samples were collected in the frequency range of 100 kHz–0.01 Hz using the signal amplitude of 10 mV. The electrochemical performance of NVP/C as the cathode material in half–cells was investigated within a voltage window of 2.0–4.25 V. The electrodes were prepared using slurry casting method (8:1:1 mass ratio of active material, Super P as conductive carbon, and PVDF as binder) on Al current collector with an average loading of approximately 1.8 mg cm^{-2}. Metallic–Na was used as counter electrode, and the C–rate was defined by setting 1C equivalent to 117 mA h g^{-1}. The cycling performance assessment was conducted with a C–rate of 0.5C. Likewise, the electrochemical performance of $K_{0.5}Mn_{0.8}Co_{0.1}Ni_{0.1}O_2$ (KMCNO) microcuboids as the K–ion cathode in half–cells was investigated within a voltage window of 1.5–4.0 V. The KMCNO microcuboids as cathode was prepared using previous report [39]. Metallic–K was used as counter electrode. The rate capability tests were examined at various current density ranging from 10 to 100 mA g^{-1}, whereas the cycling test was conducted at a current density of 20 mA g^{-1}. Na–ion full cells were assembled by incorporating Se@P–N–C@Mo_2C as the anode and NVP/C as the cathode separated by GF, with a fixed voltage window of 0.5–3.8 V. The cycling performance was evaluated at a C–rate of 0.1C. Noteworthy is the pre-assembly step, where the half–cell featuring Se@P–N–C@Mo_2C anodes underwent a single charged/discharged cycle at 0.1C–rate. The recovered sodiated anode, carefully handled within a glove box, was then employed in the assembly of the full cell. Moreover, the active material loading in the cathode and anode electrodes was adjusted to achieve a negative/positive (N/P) ratio of 1.0. Similarly, K–ion full–cells were also assembled using Se@P–N–C@Mo_2C as the anode and KMCNO as the cathode separated by GF, with a fixed voltage range of 0.5–3.7 V. The cycling performance was evaluated at a current density of 20 mA g^{-1} in 1.0 M KPF_6 dissolved in 1, 2 dimethoxyethane (DME). The N/P ratio for full cell was adjusted to 1.1.

2.5. Computational methodology

Spin-polarized DFT calculations were performed using the Vienna Ab-initio Simulation Package (VASP) [40–43]. These calculations employed projected-augmented wave (PAW) pseudopotentials and the Perdew–Burke–Ernzerhof (PBE) exchange–correlation functional with the generalized gradient approximation (GGA) to describe core–valence interactions [44,45]. A plane-wave cutoff energy of 520 eV was employed [46]. To prevent interactions between different nearest neighboring layers, a vacuum space of 20 Å was introduced along the Z-direction. Brillouin zone sampling was implemented using a Γ-centered Monkhorst-Pack with k-mesh of 9 × 9 × 4 for Mo_2C bulk calculations, and 2 × 4 × 1 k-point grids for (6 × 3) Mo_2C(101) surface calculations, respectively [47]. The adsorption energy of polyselenides such as Se_8, Na_2Se_6, Na_2Se_4, and Na_2Se on the (6 × 3) Mo_2C(101) surface was calculated using following equation:

$$E_{ads} = E_{adsorbate@surface} - E_{surface} - E_{adsorbate} \quad (1)$$

Here, $E_{adsorbate@surface}$ represents the total energy of the adsorbate adsorbed surface, $E_{surface}$ represents the energy of the surface slab, and $E_{adsorbate}$ is the energy of adsorbate, respectively. A more negative adsorption energy corresponds to a stronger binding between the adsorbate and the catalytic surface, rendering E_{ads} valuable for characterizing activity trends and relative energetics.

3. Results and discussion

3.1. Physical characterization of the prepared powders

The as-spun fibers, which were stabilized at 150 ℃, were subjected to comprehensive analysis for morphological and phase determinations. The continuous fibrous morphology of the stabilized fibers, depicted in Fig. 1a through field-emission scanning electron microscopy (FE-SEM) micrograph, exhibited an average diameter of ~1.0 μm and smooth fiber surface, indicating the effective confinement of all constituents within the fiber. The cross-sectional image (Fig. 1b) displayed the uniform dispersion of Mo-salt as well as elongated PS within the PAN polymer. Notably, the different solubility degrees of the PS component compared with those of PAN in a DMF solvent facilitated the formation of an atoll-like shape, which stretched under a high electric field in the spinning process [48]. The X-ray diffraction (XRD) pattern (Fig. 1c) revealed the amorphous nature of the stabilized NFs, with a distinct peak at approximately $2\theta = 16.7°$, which was attributed to the PAN polymer. Subsequently, the stabilized Mo-salt/PS/PAN composite fibers underwent carbonization at 800 °C in the N_2 atmosphere (Fig. 1d–f). The FE-SEM micrograph (Fig. 1d) indicated the preservation of the fibrous morphology (albeit with a decreased average diameter of ~0.8 μm due to NF shrinkage during the high-temperature treatment) attributed to the removal of highly volatile constituents, such as the elongated PS phase. Notably, PAN transformed into an N-doped carbonaceous species (N–C) during carbonization, facilitated by the N-rich organic units

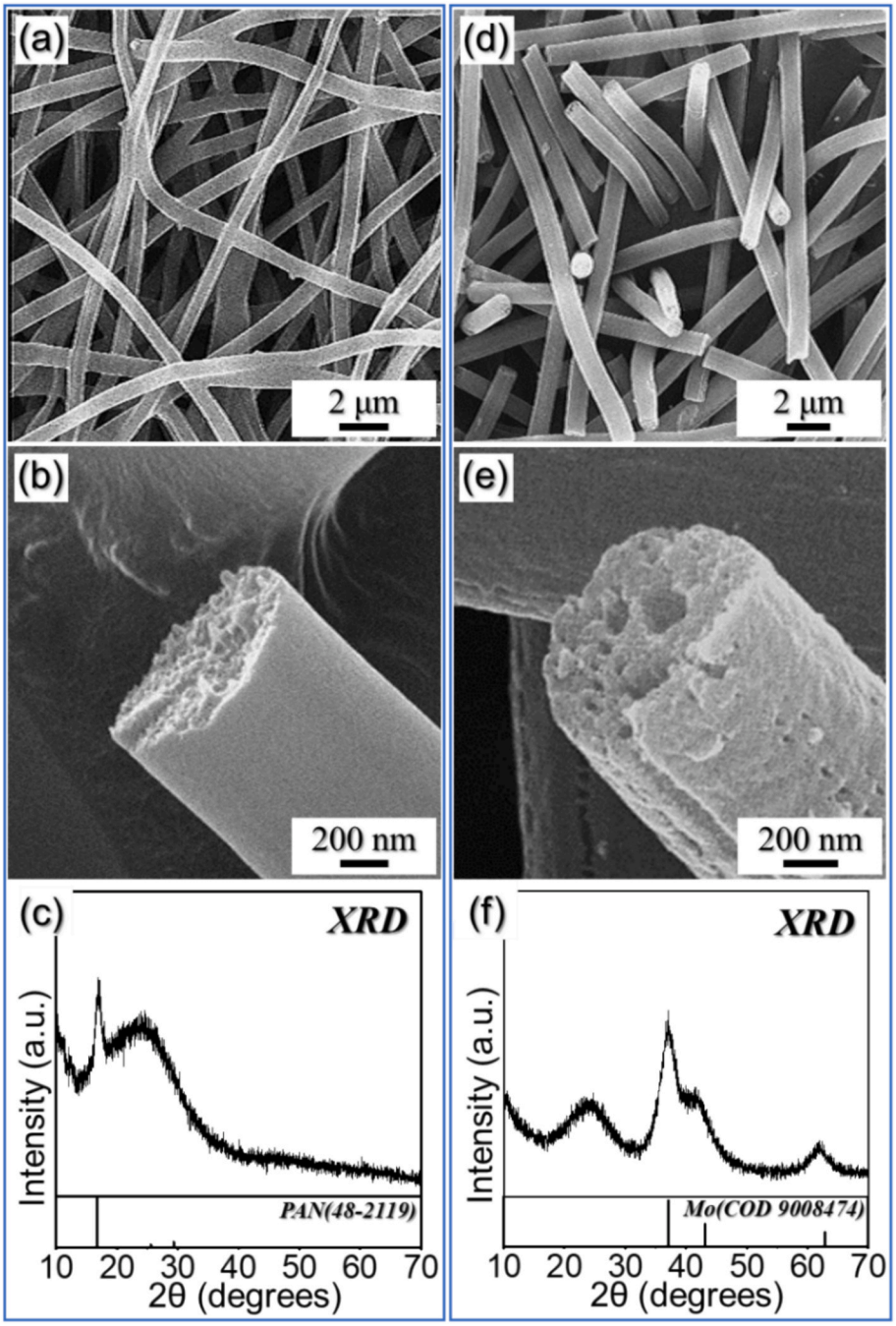

Fig. 1. FE–SEM and XRD pattern of the (a–c) as-spun Mo-salt/PS/PAN composite fibers stabilized at 150 °C and (d–f) P–N–C@Mo NFs obtained after carbonization of stabilized composite fibers at 800 °C in an N_2 atmosphere: (a, d) FE–SEM images, (b, e) cross-sectional FE–SEM images, and (c, f) XRD patterns.

[–(C_3H_3N)–] within the PAN polymer. The high-magnification FE-SEM cross-sectional image (Fig. 1e) revealed the presence of long-range porous tunnels along the fiber length, which were formed by the complete thermal decomposition of the elongated PS phase during carbonization. Additionally, the micrograph emphasized numerous macro-sized openings within NF. These continuous longitudinal tunnels facilitated the efficient electrolyte infiltration and decreased the effective diffusion length of the charged species. The porous characteristics contributed significantly to the enhancement of the overall electrochemical performance. The XRD pattern (Fig. 1f) displayed broad peaks that are associated with the pristine Mo phase (*Cubic* crystal; $Fm\bar{3}m$ space group), with ultrafine morphological characteristics. Additionally, a broad peak at approximately $2\theta = 23.9^{\circ}$ was linked to PAN-derived carbonaceous species in the nanostructure. Overall, the carbonization process yielded a porous, N-doped carbon framework with well-embedded ultrafine Mo catalysts, hereafter referred to as P–N–C@Mo NFs.

The obtained P–N–C@Mo NFs were subsequently treated with KOH at 800 °C. This step is crucial to the formation of micropores within the carbonaceous framework, a necessity for achieving high active-material loading (Se in this case). The FE-SEM micrograph (Fig. 2a) revealed that the porous morphology remained intact even after KOH activation. The magnified FE–SEM micrograph (inset of Fig. 2a) indicated that the porous longitudinal channels also maintained their form. Unexpectedly, the XRD pattern (Fig. 2b) displayed a high-intensity broad peak at $2\theta = 21.9^{\circ}$ related to the carbonaceous framework, flanked by diffraction

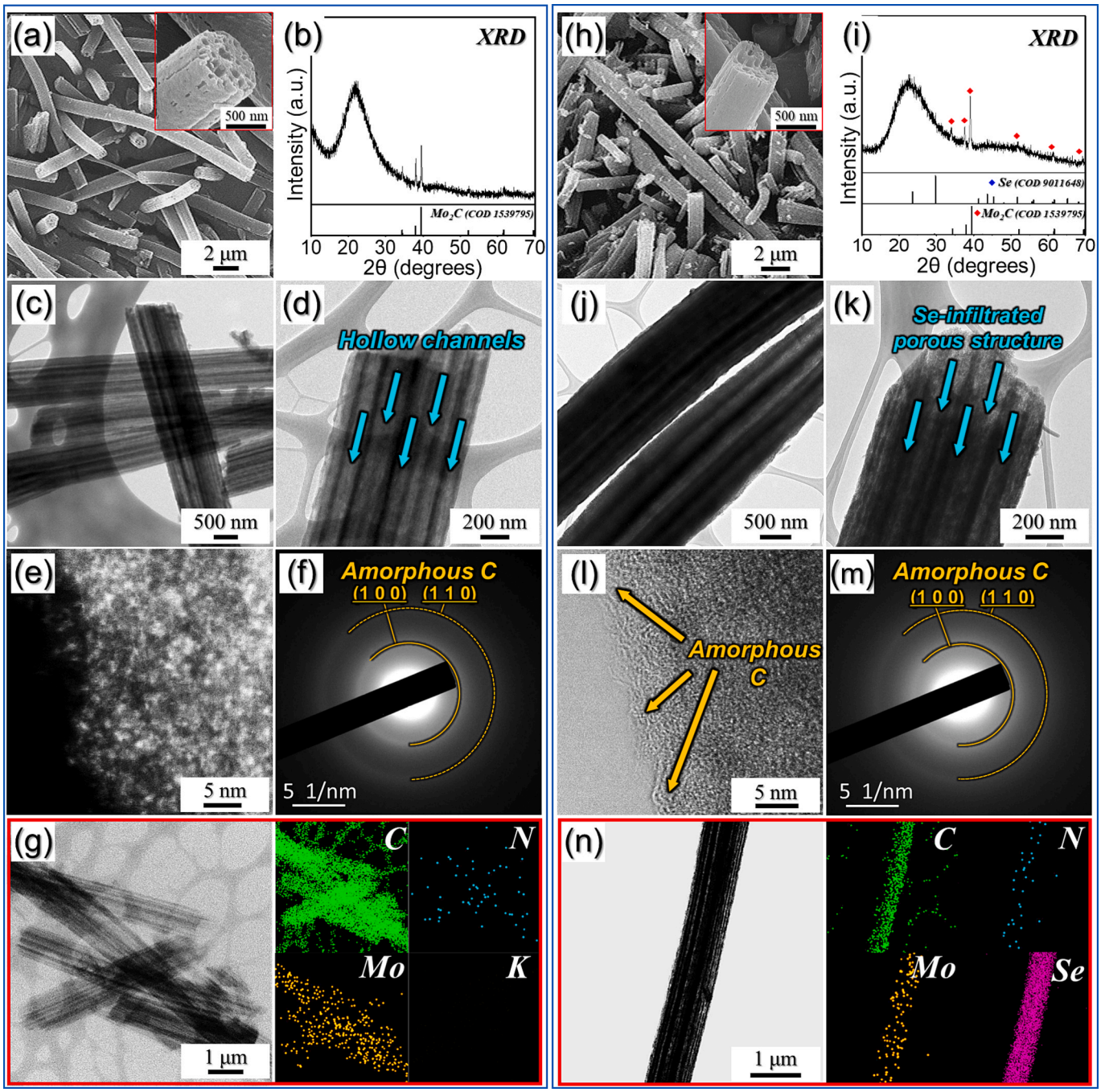

Fig. 2. FE–SEM, XRD, and TEM results of the (a–g) P–N–C@Mo_2C and (h–n) Se@P–N–C@Mo_2C NFs: (a, h) FE–SEM images, (b, i) XRD patterns, (c, d and j, k) TEM images, (e) HAADF–STEM and (l) HR–TEM images, (f, m) SAED patterns, and (g, n) elemental mapping images.

peaks corresponding to the Mo_2C phase (*Hexagonal* crystal; *P63/mmc* space group), instead of pure Mo (as shown in Fig. 1f). The conversion of the Mo_2C from Mo phase was mainly induced by KOH, which acted as a catalyst or reactive agent to decrease the formation energy of Mo_2C [49]. The transmission electron microscopy (TEM) images (Fig. 2c and d) confirmed the presence of porous longitudinal tunnels (highlighted by arrows), which were formed by the thermal decomposition of the elongated PS phase. These continuous channels support the fast diffusion of charged species by lowering the effective diffusion length while enhancing electrolyte infiltration within the sample. The HAADF–STEM image in Fig. 2e reveals the presence of numerous ultrafine nanocrystals well-embedded within amorphous carbonaceous framework. The elemental dot mapping image (Fig. S1) obtained through HAADF–STEM reveals that the uniformly distributed nanocrystals are mainly Mo-species thus confirming the formation of Mo_2C. Selected-area electron diffraction (SAED) pattern in Fig. 2f also shows diffraction rings corresponding to the amorphous carbonaceous species only thus revealing presence of thick carbonaceous species around Mo_2C nanocrystals. The mapping images (Fig. 2g) revealed the uniform dispersion of C, N, and Mo elements, suggesting the formation of ultrafine Mo_2C crystals in N-doped carbonaceous framework (labeled as "P–N–C@Mo_2C" NFs). Moreover, no K-related impurities were seen, suggesting complete removal during repeated washing. The KOH-activated P–N–C@Mo_2C NFs were further employed as a host material for Se infiltration *via* selenization process. Fig. 2(h-n) summarizes the physical characterization of the Se-infiltrated P–N–C@Mo_2C (hereafter referred to as Se@P–N–C@Mo_2C NFs). The FE–SEM micrograph (Fig. 2h and inset) did not reveal any significant changes in the 1D porous morphology, as the porous longitudinal tunnel-like channels remained intact. The XRD pattern (Fig. 2i) displays similar diffraction peak characteristics as observed in Fig. 2b, with peaks corresponding to the amorphous carbonaceous species and Mo_2C catalysts. Notably, the peak corresponding to the carbon matrix broadens, primarily due to the filling of Se [14]. Besides, no additional peaks related to bulky Se deposits were observed, indicating the amorphous nature of the Se with complete impregnation into the micropores. This observation aligns well with previous reports on Se infiltration [9,12–15]. This is further explained in detail using Raman data discussed later. Additionally, the TEM images (Fig. 2j) corresponded well with the FE–SEM results, with no observation of bulky Se deposits. This observation is more evident from the

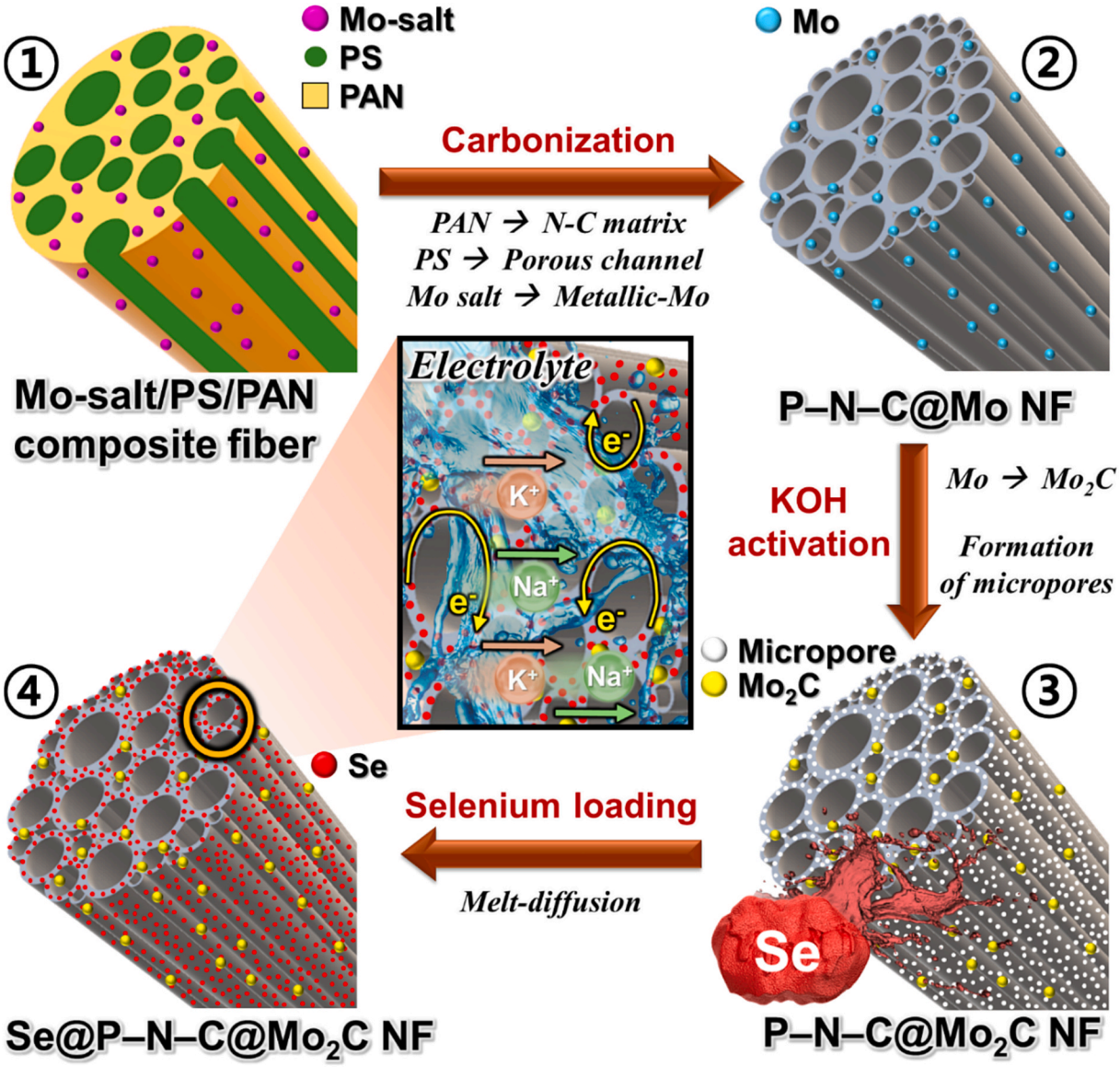

Scheme 1. Detailed illustration of the formation mechanism for Se@P–N–C@Mo_2C NF via multistep process including electrospinning (1-①), carbonization (1-②), and KOH activation (1-③), followed by melt-diffusion for selenium impregnation (1-④).

high-magnification TEM image (Fig. 2k), which revealed that the porous channels (highlighted by arrows) have become less opaque. The HR–TEM image (Fig. 2l) also confirmed the absence of any crystalline fringes, indicating the amorphous nature of the impregnated Se, which corresponded well to the XRD pattern (Fig. 2i). The SAED pattern (Fig. 2m) further revealed diffraction rings that corresponded to the amorphous carbonaceous species. The elemental dot maps (Fig. 2n) revealed the homogenous dispersions of the C, N, Mo, and Se elements in the 1D framework, indicating the efficacious synthesis of Se@P–N–C@Mo_2C NFs. The high concentration and low density of C and N, respectively, in the sample correlated well with the elemental analysis (EA) results (Table S1), indicating ~28 wt% of C and 0.68 wt% of N. Furthermore, the sparse distribution of Mo suggests a low content. To verify this, a thermogravimetric (TG) curve was obtained for Se@P–N–C@Mo_2C NFs in an air atmosphere (Fig. S2). The residue after 700 °C was ~7.4 wt%, indicating the presence of Mo species within the prepared nanostructure. Additionally, the dot mapping images corresponding to the Se element indicated its considerable proportion in the prepared sample. The TG curve (Fig. S3) revealed that the Se content impregnated in Se@P–N–C@Mo_2C was ~58 wt%.

The synthesis process of Se@P–N–C@Mo_2C NFs involves a multi-step procedure, as systematically depicted in Scheme 1. Initially, as-spun composite fibers are formed, containing uniformly distributed Mo-salt and atoll-like PS phase within a PAN matrix (Scheme 1-①). The as-spun composite fibers are then stabilized at 150 °C under ambient conditions, followed by carbonization at 800 °C (Scheme 1-②). During carbonization, the atoll-like PS phase completely decomposes, forming tunnel-like marcoporous channels along the fiber length. Simultaneously, the PAN matrix carbonizes to form a nitrogen-rich carbonaceous (N–C) framework. Additionally, the Mo-salt reduces to pure metallic-Mo catalysts, homogeneously distributed within the N–C framework. The presence of the carbon matrix surrounding the Mo catalysts restricts grain growth and prevents aggregation, thus resulting in the formation of ultrafine Mo catalysts. Consequently, the

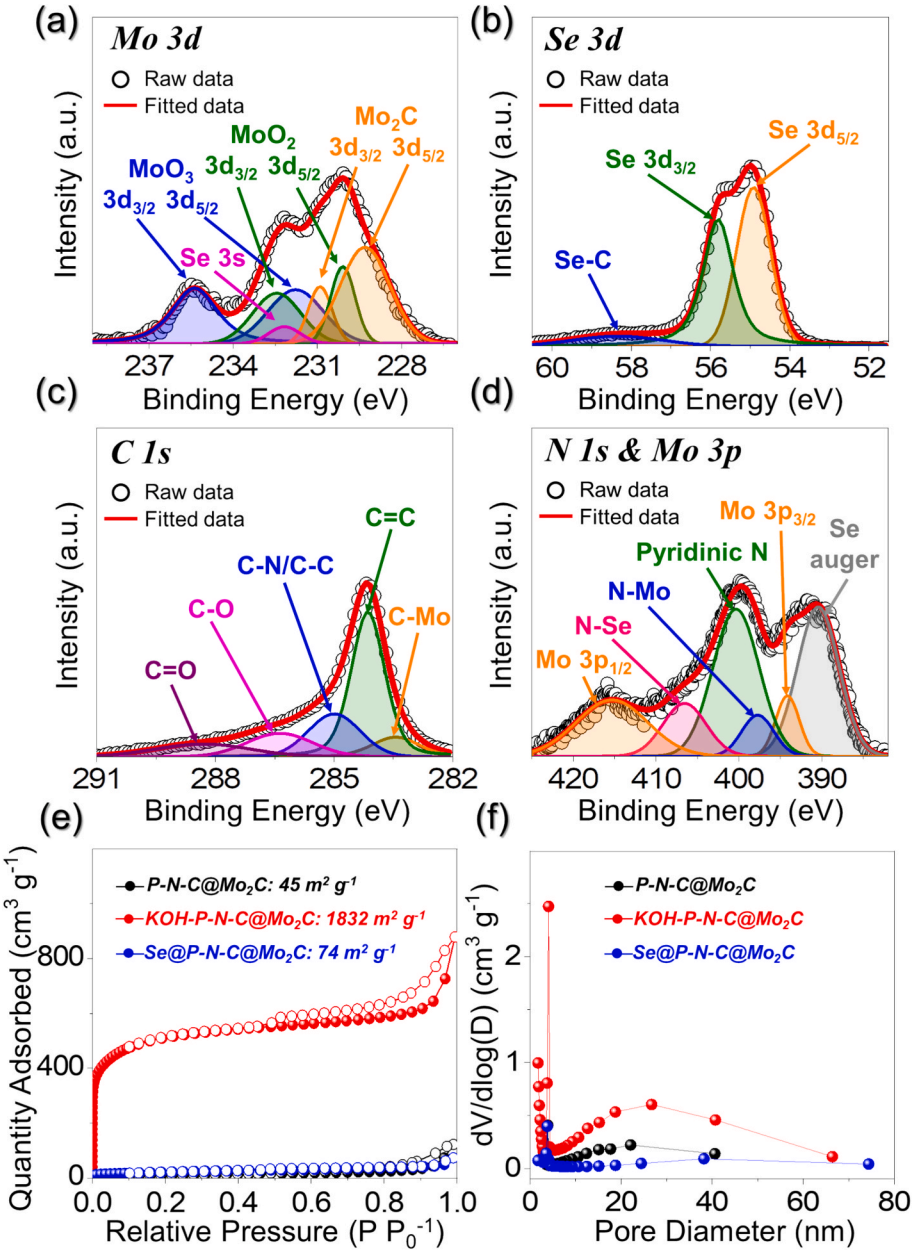

Fig. 3. XPS analysis of Se@P–N–C@Mo_2C NFs: (a) Mo 3*d* deconvoluted XPS, (b) Se 3*d* deconvoluted XPS, (c) C 1*s* deconvoluted XPS, (d) N 1*s* and Mo 3*p* deconvoluted XPS; (e) N_2 adsorption–desorption isotherms, and (f) BJH pore-size distribution of nanofibers at different stages of synthesis.

carbonization step yields one dimesional, porous, and N-rich carbon nanofibers comprising well-embedded ultrafine metallic-Mo catalysts (P–N–C@Mo NF). The obtained carbonized NFs underwent a chemical activation process using KOH (Scheme 1-③), followed by washing. This step guarantees the formation of micropores within the N–C framework, along with mesopores, which subsequently aids in high active-material impregnation. Additionally, the KOH treatment facilitates the phase conversion from ultrafine metallic-Mo to Mo_2C catalyst, resulting in the formation of P–N–C@Mo_2C NF. Finally, the Se impregnation step is performed using elemental Se and P–N–C@Mo_2C NF in a 2:1 mass ratio, heated at 260 °C and following 350 °C in an N_2 atmosphere, to fill the micropores with Se (Scheme 1-④). This step resulted in the formation of Se-impregnated highly porous and N-rich NFs, comprising uniformly distributed ultrafine Mo_2C catalysts (Se@P–N–C@Mo_2C NF). The porous structure ensures enhanced structural integrity, efficient diffusion of charged species (magnified Scheme 1-④), better electrolyte percolation, and effective volume accomodation, crucial for improved electrochemical performance.

The valence state and surface compositions of the various elements in Se@P–N–C@Mo_2C NFs were characterized by X-ray photoelectron spectroscopy (XPS). The XPS survey spectrum (Fig. S4) displayed distinct photoelectron peaks corresponding to N 1*s*, C 1*s*, Mo 3*d*, and Se 3*d*. The intense peak corresponding to the Mo 3*d* profile at 230.1 eV (Fig. 3a) was delineated into two well-separated peaks at 229.3 and 230.9 eV, corresponding to the Mo $3d_{5/2}$ and Mo $3d_{3/2}$ orbitals, respectively. These peaks were attributed to the characteristic spin doublet associated with the Mo^{2+} species inherent to β-Mo_2C [50]. Additionally, the peak pairs presents at 230.0/232.4 and 232.1/235.3 eV were attributed to the Mo^{4+} and Mo^{6+} states, respectively, in MoO_2 and MoO_3, indicating the surface oxidation of the Mo_2C nanocrystals during the analysis [51,52]. Further, the less distinct peak at 232.1 eV was attributed to the metalloid Se (Se 3*s*) infiltrating the nanostructure during selenization [53,54]. The deconvoluted Se 3*d* spectrum (Fig. 3b) revealed two prominent peaks at 54.9 and 55.8 eV, corresponding to the Se $3d_{5/2}$ (terminal Se; Se_T^{-1}) and Se $3d_{3/2}$ (bridge Se; Se_B^0) orbitals, respectively [2,53]. Furthermore, a broad, lower-intensity peak at 58.3 eV was associated with the Se–C species, indicating the interaction between the infiltrated Se and carbon species [54]. The absence of a Se–C peak in the XPS spectrum of the elemental Se powder (Fig. S5) firmly confirmed the above observation. In the deconvoluted C 1*s* spectrum (Fig. 3c), five well-resolved peaks were observed at 283.4, 284.1, 284.9, 286.3, and 288.3 eV, corresponding to the –C–Mo–, sp^2-bonded –C═C–, sp^3-bonded –C–N/C–C–, CO, and –C═O– species, respectively [38,48,50,55]. The highest intensity of the –C═C– peak corresponded to a significant proportion of the carbonaceous species within the nanostructure [56–58]. Additionally, the presence of the –N–C– peak confirmed N-doping in the carbonaceous framework [59–61]. N-doping substantially enhanced the electronic conductivity of the nanostructure due to the high electronegativity of nitrogen [62–64]. The deconvoluted N 1*s* spectrum (Fig. 3d) corroborated the above observations. The spectrum displaying well-fitted peaks at 390.4, 394.1, 397.7, 400.3, 406.5, and 415.3 eV, attributed to Se (LMM) Auger electrons from Se metalloid, Mo $3p_{3/2}$ species, –Mo–N species, pyridinic N, –Se–N species, and Mo $3p_{1/2}$, respectively [65–70]. Notably, –Mo–N and –Se–N bonds appeared because of the interaction between Mo/Se and N-doped carbonaceous species [51,71]. The EA analysis of C and N (Table S1) correlated well with the XPS results. To further explore the carbonaceous structure of the nanostructure, Raman analysis was performed and interpreted. The Raman spectrum of Se@P–N–C@Mo_2C NFs (Fig. S6a) displayed typical D- and G-band signatures at 1347 and 1594 cm^{-1}, respectively. The intensity ratios of both bands (~1.02) confirmed the amorphous nature of the carbonaceous species [72]. Additionally, a peak at 245 cm^{-1} was attributed to the Se–Se bond in the nanostructure [12]. Moreover, the magnified Raman spectrum (Fig. S6b) indicated that the primary Se peak comprised three closely spaced peaks corresponding to ring-Se (*r*-Se), chain-Se (*c*-Se), and trigonal-Se (*t*-Se) at 270.4, 245, and 234.0 cm^{-1}, respectively [12]. Remarkably, the shift of the *c*-Se peak to high wavenumber values compared with elemental Se (Fig. S6e and f; 233 cm^{-1}), along with the significant decrease in the intensity, indicates the transformation from crystalline to amorphous Se during the impregnation process [14]. This observation is consistent with the XRD results presented in Fig. 2i. Furthermore, the substantial peak intensity corresponding to *c*-Se was attributed to a higher degree of short-range ordering, a common phenomenon in Se-based nanostructures [73]. Additionally, the intense signature of *c*-Se indicated that a more significant amount of active material would participate in redox processes to ensure superior electrochemical performance. It's noteworthy to mention that the presence of N-doping in the nanostructure, as predicted by EA and XPS, induced beneficial defects that contribute to enhancing the performance of the cell. Fig. 3e and f show the changes in the surface area (N_2 adsorption–desorption isotherms) and Barrett–Joyner–Halenda pore-size distribution of the as-prepared NFs at different synthesis stages, i.e., before and after KOH activation and after Se infiltration. The surface area increased significantly from 45 to 1832 $m^2\ g^{-1}$ after KOH activation, attributed to a substantial increase in the micropore (Fig. S7) and mesopore (Fig. 3f) volumes after KOH treatment. Moreover, a drastic decrease in the surface area (74 $m^2\ g^{-1}$) after Se impregnation indicated micropore filling. Notably, the effective confinement of Se within the micropores impeded the diffusion of Na/K–PSes toward the anode, facilitating high active-material utilization. To highlight the structural merits of Se@P–N–C@Mo_2C NFs, we prepared a comparison sample using a similar synthesis technique but without the Mo precursor. Fig. S8 shows the FE–SEM micrographs and XRD patterns of the as-spun PAN/PS composite fibers, stabilized at 150 °C along with the carbonized NFs (P–N–C NFs), and followed by the relevant discussion. Similarly, Fig. S9 show the physical characterizations and respective discussions on the KOH-treated carbonized NFs along with Se-impregnated KOH-treated carbonized (Se@P–N–C) NFs.

3.2. Electrochemical performance of the prepared powders for Na–Se batteries

Motivated by the exceptional physicochemical properties, we comprehensively explored the inherent energy-storage capabilities of Se@P–N–C@Mo_2C and Se@P–N–C NFs, and the findings succinctly summarized in Fig. 4. The cyclic voltammetry (CV) curves were first obtained at a voltage scan rate of 0.1 mV s^{-1} and analyzed for the redox processes occurring within the cells. The first CV scan (Fig. 4a) within the voltage window of 0.5–3.0 V revealed distinct reduction peaks at 1.98 and 1.09 V for Se@P–N–C@Mo_2C contrary to 2.12 and 1.35 V for Se@P–N–C NFs. The reduction peaks appearing at the higher voltage range for both samples (marked by black and red arrows) were attributed to the transformation of *r*-Se → *c*-Se, analogous to the phenomenon observed in Li–Se batteries [12]. Notably, the absence of these peaks during consecutive redox cycles (Fig. 4b and c) indicated the complete transformation from *r*-Se → *c*-Se during the first cycle. Furthermore, the sharp cathodic peaks in the low-voltage range for both samples were linked to the subsequent conversion of *c*-Se to Na_2Se (*c*-Se + $16Na^+$ + $16e^-$ → $8Na_2Se$) [74]. In the anodic scan, a solitary intense peak emerged at ~1.76 and 1.89 V, indicating the oxidation of Na_2Se into Se (xNa_2Se → Se + $2xNa^+$ + $2xe^-$), thereby completing the redox cycle. Significant changes were observed in the subsequent reduction cycles, particularly during the reduction process for the cell employing the Se@P–N–C@Mo_2C electrodes. Dissimilar to the single sharp cathodic peak at 1.09 V in the first cycle, the peak split into two closely spaced peaks from the second cathodic scan, indicating a two-step reaction process. The shoulder peak at ~1.36 V was attributed to the transformation of *c*-Se, which was formed during the first discharge, into an intermediate PSe phase (*c*-Se + $2Na^+$ + $2e^-$ → Na_2Se_n). The primary peak at 1.12 V confirmed the further reduction of intermediate PSes (Na_2Se_n) into the final discharge product, i.e., Na_2Se (Na_2Se_n + (2n − 2)

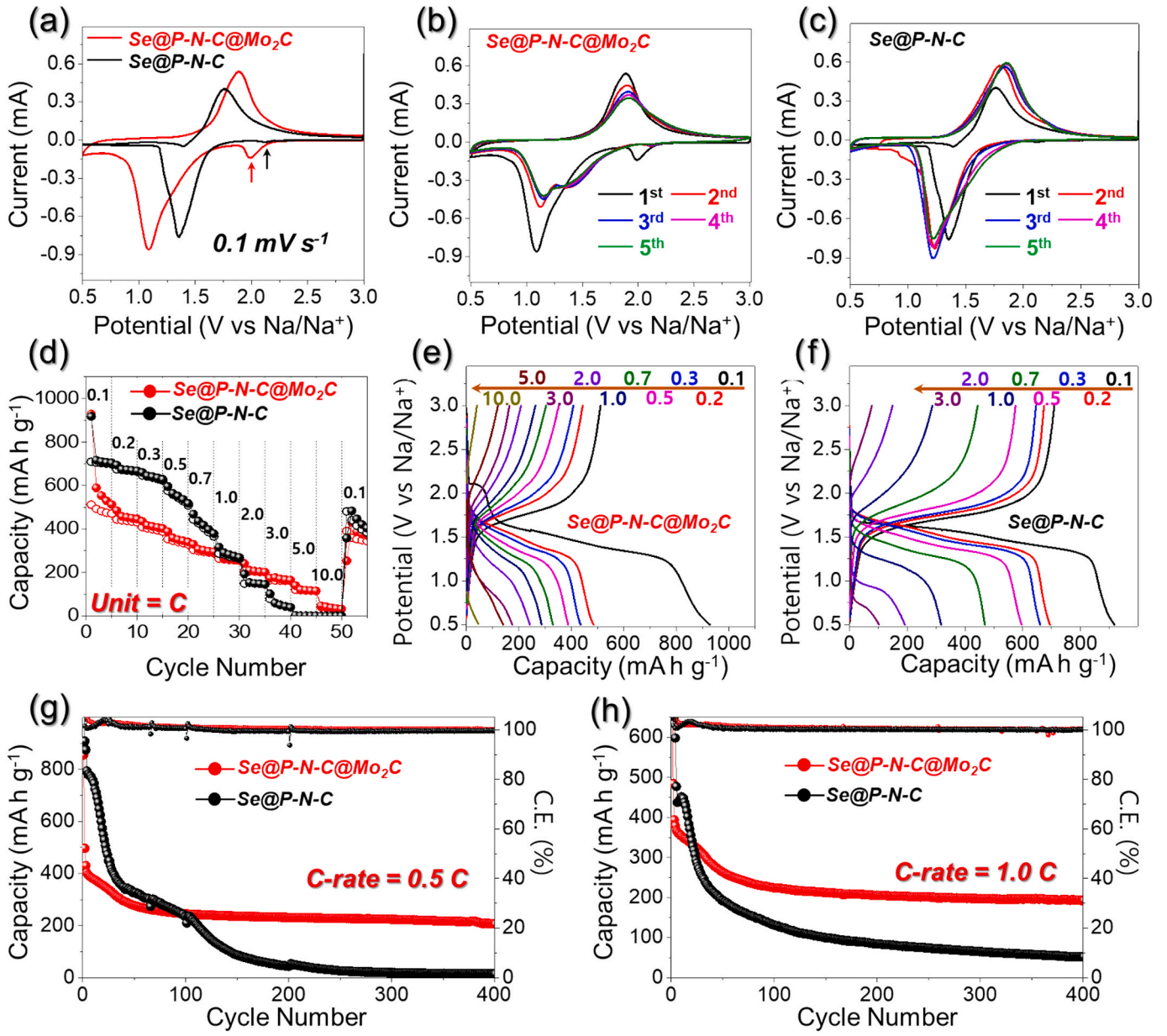

Fig. 4. Electrochemical performance of Se@P–N–C@Mo_2C and Se@P–N–C NFs for Na–ion storage: (a) First CV scan comparison at 0.1 mV s^{-1}, (b) First five CV scans for Se@P–N–C@Mo_2C NFs at 0.1 mV s^{-1}, (c) First five CV scans for Se@P–N–C NFs at 0.1 mV s^{-1}, (d) Rate capability tests at different C–rates ranging from 0.1 to 10.0C, (e) Galvanostatic voltage profiles for Se@P–N–C@Mo_2C NFs at different C–rates, (f) Galvanostatic voltage profiles for Se@P–N–C NFs at different C–rates, (g) Cycling performance at a C–rate of 0.5C, and (h) Cycling performance at a C–rate of 1.0C.

$Na^+ + (2n - 2)e^- \rightarrow nNa_2Se$). Notably, such a distinct phenomenon was not observed for the cell utilizing the Se@P–N–C electrode, and this indicated the one-step conversion of *c*-Se into Na_2Se. Remarkably, the redox intensity peaks were higher for the Se@P–N–C electrode (Fig. 4c), indicating better redox kinetics initially. This could be attributed to several factors, including the highly porous structure (Fig. S9) and relatively high N content (Table S1) of the sample compared with the Se@P–N–C@Mo_2C NFs, which facilitated the better diffusion of charged species along with faster redox processes. However, the initial enhancement of electrochemical performance for the Se@P–N–C electrode was not sustained throughout (as will be discussed shortly) and decreased drastically at a later stage of electrochemical testing. Additionally, the firmly overlapped and symmetric CV curves indicated the occurrence of highly reversible redox processes. Overall, the CV results indicated improved redox properties due to the synergistic effects of the various components within the prepared nanostructure.

To assess the values of the practical discharge capacity from the CV curves–predicted redox processes, Se@P–N–C@Mo_2C and Se@P–N–C cathodes were subjected to rate-capability tests at diverse current rates (C-rates) ranging from 0.1 to 10.0C (Fig. 4d), with 1C being equal to 675 mA h g^{-1}. As anticipated by the CV predictions, the cell comprising the Se@P–N–C cathode exhibited higher discharge capacities, up to 1.0C, which sharply decreased afterward, approaching zero capacity values at high C-rates (5.0 and 10.0C). Conversely, the Se@P–N–C@Mo_2C cathode initially delivered lower discharge capacity values but maintained stability even at high C-rates of 5.0 and 10.0C. Correspondingly, the cells employing Se@P–N–C@Mo_2C and Se@P–N–C cathodes yielded discharge capacities of 929/917, 485/694, 435/660, 388/596, 329/468, 286/316, 241/192, 174/101, 139/3, and 46/0 mA h g^{-1} at C- rates of 0.1, 0.2, 0.3, 0.5, 0.7, 1.0, 2.0, 3.0, 5.0, and 10.0C, respectively. When the current polarity was switched to 0.1C, Se@P–N–C@Mo_2C fairly recovered discharge capacity value. The considerably high discharge

capacities of the Se@P–N–C@Mo_2C cathode, particularly at high C-rates, can be attributed to several structural merits: (1) the efficient confinement of Se within the KOH-derived micropores, thereby suppressing the diffusion of PSes toward the anode; (2) the availability of 1D continuous porous channels, facilitating the smooth diffusion of charged species and accommodating large volume fluctuations; (3) smooth electrolyte infiltration, effectively wetting the electrode; and (4) the availability of chemisorption sites in the form of ultrafine Mo_2C catalyst, facilitating the effective trapping of PSes within the cathodic domain. These observations align with the respective galvanostatic charge–discharge (GCD) voltage profiles of the Se@P–N–C@Mo_2C (Fig. 4e) and Se@P–N–C cathodes (Fig. 4f). The Se@P–N–C@Mo_2C cathode displayed distinct discharge-voltage plateaus, even at high C-rates, demonstrating higher discharge capacities than the Se@P–N–C cathode. These results confirm that the synergistic effects of different structural properties contributed to the improvement of the electrochemical properties.

The sustained cycling performance represents a crucial parameter for the widespread applicability of the prepared nanostructure. The stable cycling performances of the cells featuring Se@P–N–C@Mo_2C and Se@P–N–C electrodes were analyzed at C-rates of 0.5C (Fig. 4g) and 1.0C (Fig. 4h). Notably, the cathodes were activated *via* cycling for two cycles at 0.1C. Fig. 4g shows that the cell featuring the Se@P–N–C cathode initially delivered high discharge capacity (874 mA h g^{-1} for first cycle) at 0.5C, although the capacity decreased monotonically to 366 mA h g^{-1} at the end of 35th cycle. Furthermore, the capacity of the cell did not stabilize even with further cycling, diminishing to insignificant values (14 mA h g^{-1}) after 400 continuous redox cycles, with an exceptionally high average capacity decay rate of 0.24 % per cycle. Conversely, the cell featuring the Se@P–N–C@Mo_2C cathode initially delivered a relatively low discharge capacity of 429 mA h g^{-1} when cycled at 0.5C. However, with continued cycling, the capacity stabilized at an astonishingly high value, 206 mA h g^{-1} (48 % retention), after the 400th cycle. This corresponded to an average capacity decay rate of 0.12 % per cycle, significantly lower than that of the Se@P–N–C cathode. Moreover, the higher CE value, 99.94 %, for the Se@P–N–C@Mo_2C cathode than 99.58 % for the Se@P–N–C cathode indicated more reversible redox processes within the cell. Similarly, cycling stability tests conducted at a C-rate of 1.0C revealed similar trends. The cell featuring the Se@P–N–C@Mo_2C cathode demonstrated much higher and stable discharge capacities (192 mA h g^{-1} after the 400th cycle with 52 % retention, 0.11 % decay rate, and 100.21 % CE) compared with the Se@P–N–C cathode (52 mA h g^{-1} with 10 % retention, 0.22 % decay rate, and 99.94 % CE after the 400th cycle). A comparison of the electrochemical performance is summarized in Table S2, evidently indicating a significant overall improvement. The excellent cycling stability of the Se@P–N–C@Mo_2C cathode further validated the kinetically favored redox processes occurring in the cell, supported by synergistic coupling between nanostructure merits.

To further investigate the enhanced redox kinetics within the cell featuring the Se@P–N–C@Mo_2C cathode, CV, electrochemical impedance spectroscopy (EIS), and galvanostatic intermittent titration technique (GITT) were performed to further investigate the enhanced redox kinetics within the cell featuring the Se@P–N–C@Mo_2C cathode (Fig. S11). The CV curves of the Se@P–N–C@Mo_2C (Fig. S11a) and Se@P–N–C (Fig. S11c) cathodes exhibited single cathodic and anodic peaks with considerable current intensities, particularly at high-voltage scan rates. However, at elevated voltage scan rates, a considerable increase in the hysteresis was observed, and it was attributed to significant polarization. Notably, the polarization potential (ΔV) values between the cathodic and anodic peaks of the Se@P–N–C@Mo_2C cathode at voltage scan rates of 0.2, 0.3, 0.5, and 1.0 mV s^{-1} were 0.79, 0.88, 0.95, and 1.12 V, respectively. Conversely, the ΔV values for the Se@P–N–C cathode increased significantly to 0.78, 0.96, 1.10, and 1.40 V, respectively, for identical scan rates. This indicated that the presence of the ultrafine Mo_2C catalyst inhibited electrode polarization, allowing for more reversible redox reactions. Besides, the catalyst provided additional chemisorption sites for the efficient catalytic conversion of trapped PSe species. Furthermore, both cathodes displayed analogous CV-curve shapes, indicating almost similar redox characteristics. The high redox intensities observed in the cathodic and anodic scans indicated high active-material utilization along with enhanced Na-ion diffusion. The diffusion properties within the cells were analyzed by the Randles–Sevcik equation, as follows:

$$Ip = 2.69 \times 10^5\, n^{1.5}\, A D_{Na^+}^{0.5}\, C_{Na} \nu^{0.5} \quad (2)$$

where the parameters have their usual meanings. The slope of the current *vs.* square root of the voltage scan-rate graph (Fig. S11b and d) was used to calculate the $D_{Na}{}^+$ values. The average $D_{Na}{}^+$ coefficient was approximately 1.2 times higher for the Se@P–N–C@Mo_2C cathode (11.2×10^{-10} cm^2 s^{-1}) than for the Se@P–N–C cathode (9.4×10^{-10} cm^2 s^{-1}), indicating better charge-transfer characteristics supported by kinetically favored redox processes. To gain deeper insights into the redox kinetics, the EIS curves of the cathodes were obtained during cycling at a C-rate of 0.5C. The obtained Nyquist plots were fitted with various components connected in series and parallel to construct an equivalent circuit (Fig. S12). R_e, R_{ct}, Q, and Z_w represent the electrolyte/solution resistance, charge-transfer resistance, constant-phase element of the electrode/electrolyte interphase, and Warburg impedance, respectively. The EIS curve (Fig. S11e and f) revealed that the cell featuring the Se@P–N–C@Mo_2C cathode demonstrated equivalent R_s values of 24, 48, 46, 55, and 73 Ω and R_{ct} values of 42, 47, 99, 187, and 172 Ω after 0 (fresh), 20, 50, 100, and 200 cycles, respectively. Conversely, the Se@P–N–C cathode realized much higher R_s values (63, 50, 76, 98, and 139 Ω, after 0 (fresh), 20, 50, 100, and 200 cycles, respectively) and R_{ct} values (98, 148, 238, 339, and 512 Ω, after 0 (fresh), 20, 50, 100, and 200 cycles, respectively). The smaller electrode and R_{ct} of the Se@P–N–C@Mo_2C cathode indicated that Mo_2C functioned as an efficient PSe reservoir, restricting shuttling, reactivating the trapped active materials, and enabling faster electrode reaction kinetics as well as a stable electrode interface structure. The GITT results, which were obtained by applying a current pulse at a 0.1C-rate for 10 min, followed by relaxation for 1 h, are shown in Fig. S11g and h, demonstrating that both cathodes exhibited similar voltage changes during Na-ion intercalation/deintercalation. Notably, the GITT results correlated well with the rate and cycling performance, particularly at the initial stage of electrochemical testing. Overall, the redox kinetic results explored using stepwise CV scan, EIS measurements during cycling, and GITT analysis demonstrated the enhanced charge-transfer characteristics of the Se@P–N–C@Mo_2C cathode owing to its porous and conductive carbonaceous skeleton along with numerous catalytic sites for the efficient trapping and conversion of PSe species.

3.3. Electrochemical performance of the prepared powders for K–Se batteries

The K-ion-storage properties of the Se@P–N–C@Mo_2C and Se@P–N–C cathodes were thoroughly analyzed, and the results are summarized in Fig. 5. The initial CV scan of the Se@P–N–C@Mo_2C/Se@P–N–C cathode (Fig. 5a) displayed three distinct reduction peaks at ~2.37/2.41 V (conversion of *r*-Se → *c*-Se), 1.52/1.46 V (formation of K_2Se_2), and 0.82/0.97 V (formation of K_2Se). However, in successive cycles (Fig. 5b and c), the peaks corresponding to *r*-Se → *c*-Se conversion and K_2Se_2 formation disappeared, indicating a direct process between Se and K_2Se, without the involvement of an intermediate polyselenide. In the reverse scan (Fig. 5a), two anodic peaks were observed at 1.90/1.85 V (K_2Se → K_2Se_2 conversion) and 2.28/2.21 V (K_2Se_2 → Se_n conversion). However, for consecutive cycles (Fig. 5b and c), only single anodic peaks were detected, indicating the direct oxidation of K_2Se → Se. The first CV scan indicated the high irreversible capacity losses for both samples, which were primarily attributed to the decomposition of the electrolyte

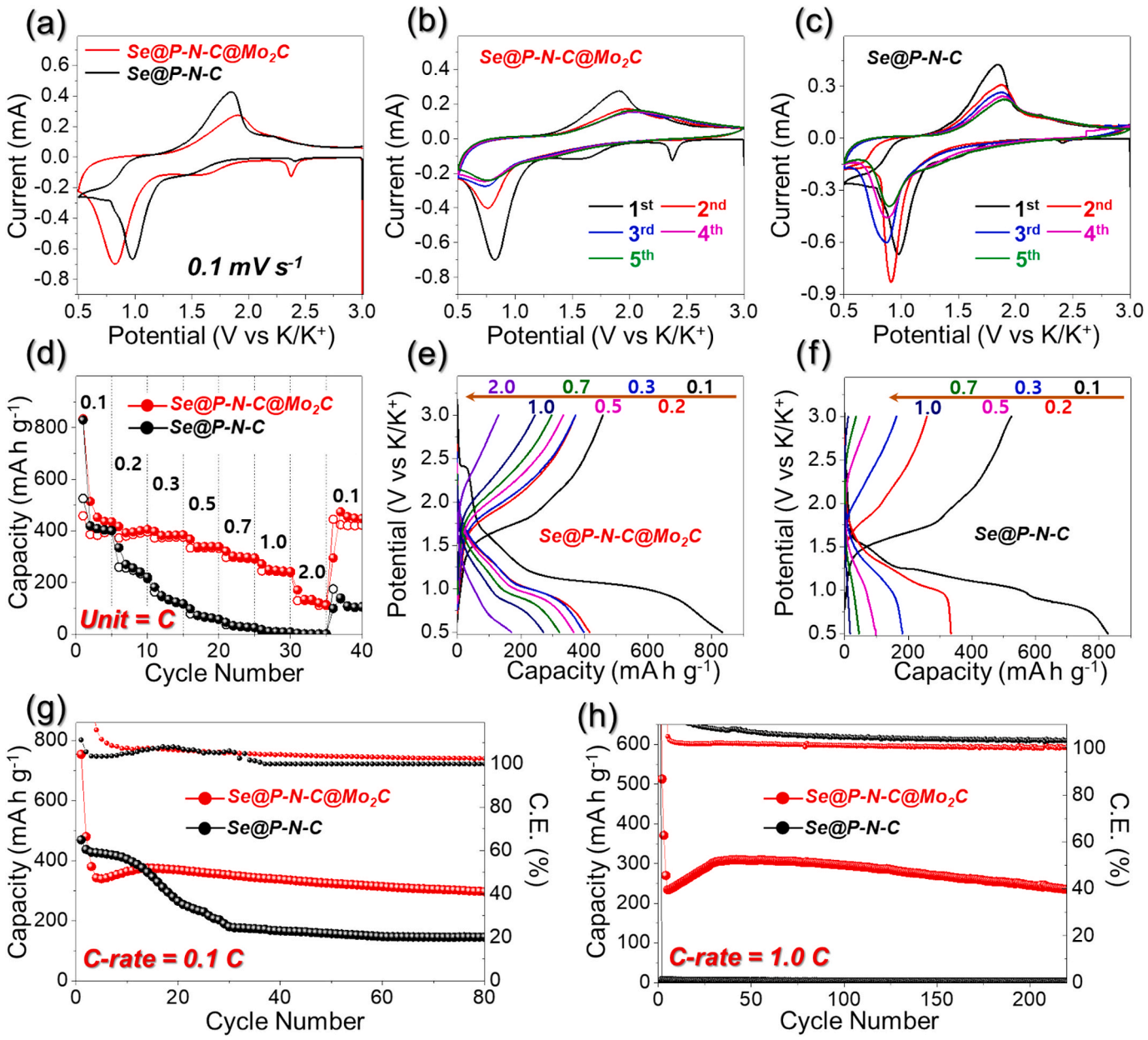

Fig. 5. Electrochemical performance of Se@P–N–C@Mo_2C and Se@P–N–C NFs for K–ion storage: (a) First CV scan comparison at 0.1 mV s^{-1}, (b) First five CV scans for Se@P–N–C@Mo_2C NFs at 0.1 mV s^{-1}, (c) First five CV scans for Se@P–N–C NFs at 0.1 mV s^{-1}, (d) Rate capability tests at different C–rates ranging from 0.1 to 2.0C, (e) Galvanostatic voltage profiles for Se@P–N–C@Mo_2C NFs at different C–rates, (f) Galvanostatic voltage profiles for Se@P–N–C NFs at different C–rates, (g) Cycling performance at a C–rate of 0.1C, and (h) Cycling performance at a C–rate of 1.0C.

and formation of the cathodic electrolyte interface (CEI) [75]. Furthermore, consecutive CV scans of the Se@P–N–C@Mo_2C cathode (Fig. 5b) exhibited almost overlapping profiles, indicating the excellent reversibility of the redox processes. Contrarily, the current intensities of the Se@P–N–C cathode (Fig. 5c) decreased continuously, indicating limited redox reactions. The CV results predicted the stable and reversible electrochemical redox reactions for the Se@P–N–C@Mo_2C cathode compared with those of the Se@P–N–C cathode. This was further confirmed by the rate capability tests (Fig. 5d), which confirmed higher discharge capacities for Se@P–N–C@Mo_2C than for Se@P–N–C cathode at all C-rates, ranging from 0.1 to 2.0C. For instance, the initial discharge capacities of the Se@P–N–C@Mo_2C/Se@P–N–C cathodes were 834/828, 416/334, 398/182, 366/97, 321/45, 271/17, and 170/0 mA h g^{-1} at 0.1, 0.2, 0.3, 0.5, 0.7, 1.0, and 2.0C, respectively. The comparison of the GCD profiles (Fig. 5e and f) justified the higher discharge capacity of the Se@P–N–C@Mo_2C cathode. Additionally, the position of the charge–discharge voltage plateaus agreed well with the CV curves. At high C-rates (2.0C), the Se@P–N–C@Mo_2C cathode still exhibited distinct voltage profiles, whereas the voltage profiles for the Se@P–N–C cathode became obscure after 0.5C, indicating the sluggish redox kinetics within the cell. These results confirmed that the presence of the ultrafine Mo_2C catalyst within the nanostructure facilitated the effective trapping and electrocatalytic conversion of PSes within the cathodic domain. The cycling performance results at 0.1C (Fig. 5g) and 1.0C (Fig. 5h) were in good agreement with the rate-capability tests. Notably, the Se@P–N–C@Mo_2C cathode demonstrated stable cycling at 0.1C- and 1.0C-rates. Specifically, at a 0.1C-rate, the cell featuring the Se@P–N–C@Mo_2C cathode exhibited a substantial discharge capacity of 297 mA h g^{-1} (78 % retention from the 3rd cycle). Conversely, the cell featuring the Se@P–N–C cathode delivered only 145 mA h g^{-1} (34 %

retention from the 3rd cycle) after 80 cycles. Similarly, at a higher C-rate of 1.0C, the Se@P–N–C@Mo_2C cathode maintained a high and stable discharge capacity of 235 mA h g^{-1} (87 % retention from the 4th cycle) after the 220th cycle. Additionally, a remarkable CE of 100.5 % signified the high reversibility of the redox processes. In stark contrast, the cell with the Se@P–N–C cathode exhibited significantly lower discharge capacities, indicating the non-compatibility of the nanostructure for reversible K-ion storage. The results of CV, rate-capability tests, and cycling stability further validated the structural superiority of the Se@P–N–C@Mo_2C cathode. This structural advantage ensured efficient charge-transfer properties, effective electrolyte percolation, enhanced active-material utilization by inhibiting PSe diffusion, and improved redox kinetics. The comparison analysis (Table S3) confirmed that the electrochemical results obtained in this study were comparable with those previously reported.

The K-ion redox kinetics within the cell featuring the Se@P–N–C@Mo_2C cathode were further explored by various techniques (Fig. S13). The CV curves of Se@P–N–C@Mo_2C (Fig. S13a) and Se@P–N–C (Fig. S13c) manifested singular cathodic and anodic peaks denoted by arrows at each voltage scan rate. Notably, low-intensity peaks (highlighted by colored circles) were observed in both cases, indicating the formation of the PSe intermediate. However, a nuanced analysis revealed a more pronounced formation of PSe intermediates in the Se@P–N–C cathodes compared with that in Se@P–N–C@Mo_2C. This observation indicated that substantial proportions of cycling generated intermediate PSes could readily migrate toward the anode owing to the absence of electrocatalytic material and the nonpolar nature of the carbon framework. This migration caused a significant loss of the active material, resulting in inferior electrochemical performance (Fig. 5). Furthermore, the high redox intensities of the Se@P–N–C@Mo_2C cathode in the cathodic and anodic scans indicated superior active-material utilization and enhanced K-ion diffusion. The slope of the current *vs.* the square root of the voltage scan-rate graph was analyzed to assess the K-ion diffusion characteristics (Fig. S13b and d). The steeper slope of the Se@P–N–C@Mo_2C cathode revealed more kinetically favored redox processes within the cell compared with that of the Se@P–N–C cathode. These findings were corroborated by the Nyquist plots obtained for both samples during cycling at 1.0C-rate (Fig. S13e and f). The EIS curves assigned the lowest R_e and R_{ct} values to the Se@P–N–C@Mo_2C cathode. For instance, after the 50th cycle, the Se@P–N–C@Mo_2C cathode cell exhibited an R_{ct} value of 138 Ω, whereas the Se@P–N–C cathode cell shows a significantly higher R_{ct} (2.3 kΩ), indicating sluggish redox processes. Additionally, the GITT results (Fig. S13g and h) mirrored the characteristics observed in Fig. S11g and h. These results further validated the improved K-ion redox kinetics and fast charge-transfer characteristics of the Se@P–N–C@Mo_2C cathode, which are primarily attributed to its nanostructure advantages.

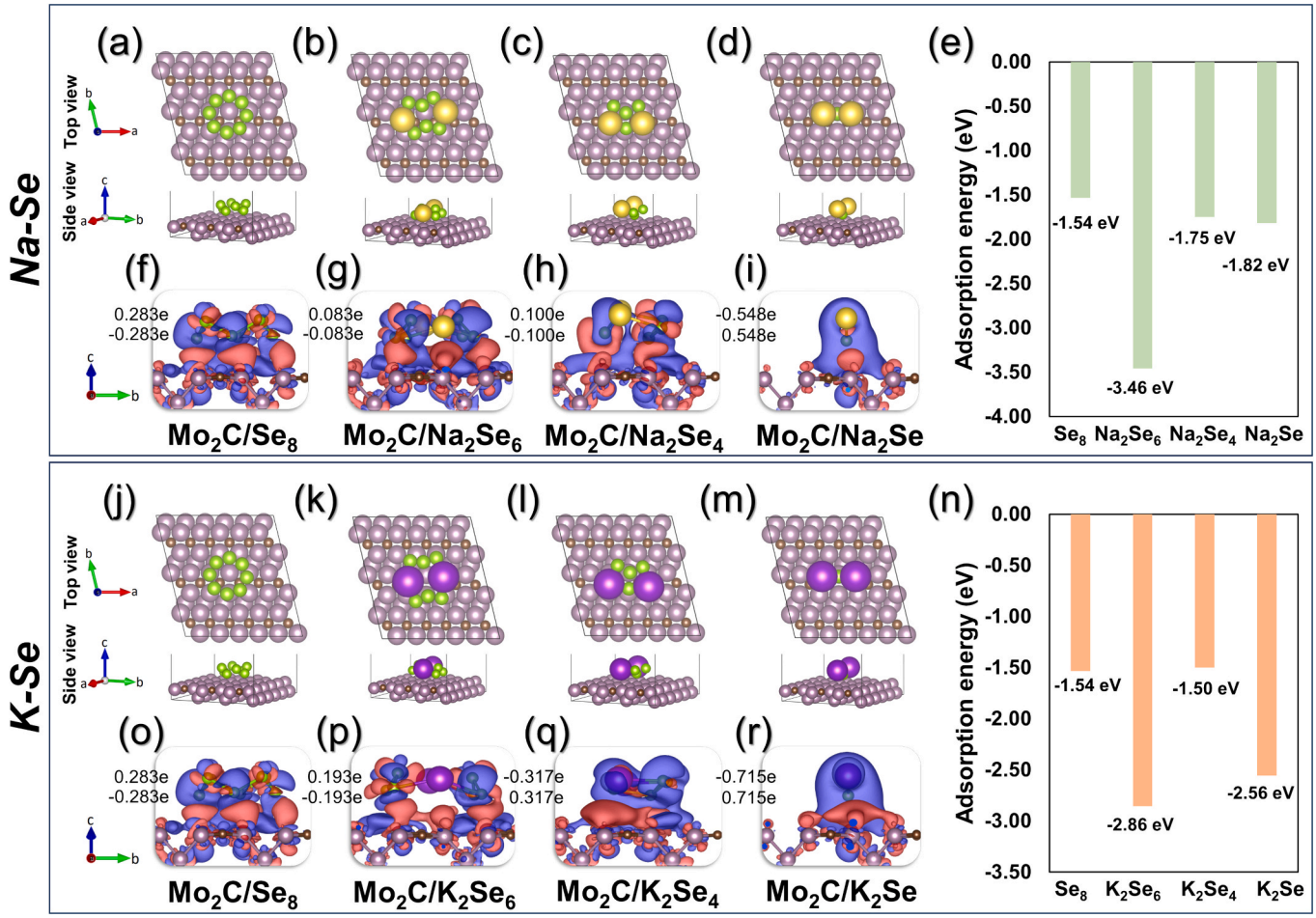

Fig. 6. Top and down panels are density functional results depicting interaction between the soluble (a–i) Na–PSes and (j–r) K-PSes with the Mo_2C surface: (a–d and j–m) Optimized structures of various polyselenide species interacting with Mo_2C. (e, n) Bar graph indicating adsorption energies of different polyselenides molecules on (6 × 3) Mo_2C(101) surface, and (f–i and o–r) Charge density difference (CDD) and excess Bader charge analysis of polyselenide species on (6 × 3) Mo_2C(101) surface (Atom color: Mo = pink, C = brown, Na = yellow, K = violet and Se = green). (For interpretation of the references to color in this figure legend, the reader is referred to the web version of this article.)

3.4. Computational insights into the Na/K–PSe adsorption capability

To validate the efficient trapping and electrocatalytic conversion of Na/K–PSes by the ultrafine Mo_2C catalyst, we performed ab initio molecular dynamic simulations, after which the corresponding adsorption energies were calculated. Fig. 6 summarizes the density functional results illustrating the interaction between soluble PSes and the Mo_2C surface. First, we designed the geometries of bulk Mo_2C (Fig. S14a) and Se (Fig. S14b), followed by the optimization of the Mo(101) surface. The bulk crystal structure of Mo_2C comprised two Mo and one C atoms, with lattice parameters ($a = b = 2.89$ Å, $c = 5.41$ Å, $\alpha = \beta = 90°$, $\gamma = 120°$), whereas the bulk Se crystal structure was composed of 32 Se atoms, with lattice parameters ($a = 9.46$ Å, $b = 10.40$ Å, $c = 15.53$ Å, $\alpha = 90°$, $\beta = 127°$, $\gamma = 90°$). Band structure calculations were executed for the Mo_2C and Se bulk structures along high symmetry *k*-points, i.e., (G-M-K-G-A-L-H-A-L-M-KH) and (G-Z-D-B-G-A-E-Z-C-Y-G), respectively. The band-structure analysis revealed that the bulk Mo_2C structure (Fig. S14c) exhibited strong electrical conductivity, with a narrow indirect band gap of 0.016 eV, bringing the valence band (VB) and conduction band (CB) closer to the Fermi level. The bandgap was calculated by the VB maximum (VBM) at 0.067 eV located at the *k*-point (0.3333, 0.3333, 0.3889) and the CB minimum (CBM) at 0.083 eV located at the *k*-point (0.1667, 0.0000, 0.5000). Similarly, the Se bulk structure (Fig. S14d) displayed an indirect bandgap of 1.637 eV, with VBM at −0.277 eV located at the *k*-point (−0.2778, 0.0000, 0.2778) and CBM at 1.360 eV located at the *k*-point (0.0000, 0.0000, 0.0000). The (6 × 3) Mo_2C(1 0 1) surface was modeled based on the experimental XRD pattern (Fig. 2i), demonstrating the highest intensity peak at approximately $2\theta = 40°$. Considering the sizes of adsorbates, such as Se_8, Na_2Se_6, Na_2Se_4, and Na_2Se, the (6 × 3) Mo_2C(1 0 1) surface can be best modeled by extending the distance to 17.32 and 18.41 Å on the *x*- and *y*-axes, respectively, with a vacuum space of 20 Å set on the *z*-axis to minimize periodic image interactions in neighboring cells. The adsorption energies of PSes, including Se_8, Na_2Se_6, Na_2Se_4, and Na_2Se, on the (6 × 3) Mo_2C(1 0 1) surface were determined to be −1.54, −3.46, −1.75, and −1.82 eV, respectively (Fig. 6a–e). The stronger adsorption energies indicated the stable interactions of PSes with the (6 × 3) Mo_2C(1 0 1) surface, effectively restricting the shuttling of the dissolved PSes between the cathode and anode. Notably, the obtained adsorption energies were higher than those previously reported for a pristine graphite surface, i.e., without any polar catalyst [25]. We performed excess Bader charge analyses to examine the Bader charge difference, following the adsorption of PSes, namely Se_8, Na_2Se_6, Na_2Se_4, and Na_2Se, on the (6 × 3) Mo_2C(1 0 1) surface (positive and negative signs indicating charge gain and loss upon adsorption) [76–78]. The redistribution of the charge density on the (6 × 3) Mo_2C(1 0 1) surface, following PSe adsorption, is illustrated by the isosurface plots of the charge-density difference (Fig. 6f–i) and examined by the following equation:

$$\Delta\rho = \rho(Mo_2C_{sur} + Polyselenide) - [\rho(Mo_2C_{sur}) + \rho(Polyselenide)] \quad (3)$$

where $\rho(Mo_2C_{sur} + Polyselenide)$, $\rho(Mo_2C_{sur})$, and $\rho(Polyselenide)$ represent the electron densities of the PSe-adsorbed (6 × 3) Mo_2C(101) surface, pristine (6 × 3) Mo_2C(101) surface, and PSes (Se_8, Na_2Se_6, Na_2Se_4, and Na_2Se), respectively. Notably, Se_8, Na_2Se_6, and Na_2Se_4 received 0.283*e*, 0.083*e*, and 0.100*e*, respectively (Fig. 6f–h), from the adsorbed surface. Conversely, regarding Na_2Se adsorption, the Mo_2C(101) surface gained 0.548*e* (Fig. 6i), owing to the electronegativity difference between the Se and Mo atoms (Mo = 2.16, C = 2.55, Na = 0.93, Se = 2.55 on the Pauling scale). This indicated that the Mo_2C(101) surface acted as an electron reservoir with a narrow bandgap. This characteristic enhanced the electrical conductivity of the electrode and could catalyze the electrode reaction. Similar results were obtained for the K–PSe adsorption analysis (Fig. 6j–r). The adsorption energies of PSes, including Se_8, K_2Se_6, K_2Se_4, and K_2Se, on the (6 × 3) Mo_2C(101) surface were determined as −1.54, −2.86, −1.50, and −2.56 eV, respectively (Fig. 6j–n). Moreover, the Bader charge analyses revealed that Se_8 and K_2Se_6 gained 0.283*e* and 0.193*e*, respectively (Fig. 6o and p), upon adsorbing onto the Mo_2C(101) surface. Conversely, for K_2Se_4 and K_2Se adsorption, the Mo_2C(101) surface received 0.317*e* (Fig. 6q) and 0.715*e* (Fig. 6r), respectively. These findings strongly confirmed that the inclusion of an ultrafine Mo_2C catalyst significantly influenced the impeding PSe migration attributed to the efficient electrocatalytic conversion facilitated by fast charge-transfer characteristics.

3.5. Sodium–selenium post-cycling analysis

To understand the factors contributing to the overwhelming electrochemical performance of the Se@P–N–C@Mo_2C cathode, we performed comprehensive post-cycling characterizations and analyses. The cells were opened in a glovebox in a fully charged state, and the components were carefully separated. The XPS and morphological changes were examined for the cycled electrode after cycling at a 1.0C-rate. The XPS survey spectrum (Fig. S15) displayed photoelectron signals corresponding to Na 1*s*, Mo 3*p*, C 1*s*, Mo 3*d*, Cl 2*p*, and Se 3*d* molecular orbitals. Notably, the Mo peaks, initially positioned at 229.3 and 230.9 eV (Fig. 3a), shifted to 228.7 and 231.1 eV (Fig. S16a), respectively, with a noticeable change in the intensity pattern. This shift indicated a possible electrophilic coupling interaction between the $Mo^{\delta+}$ and Se_x^{2-} in the Mo_2C and Na_2Se_x species, respectively. Additionally, the considerable decrease in the intensity of the Se 3*s* peak at 232.3 eV compared with that of the pristine sample (Fig. 3a) indicated that more Na_2Se_x ($4 \leq x \leq 8$) were adsorbed on the P–N–C@Mo_2C surface owing to its strong adsorption capability. Similarly, the Se 3*d* XPS spectrum (Fig. S16b) displayed similar trends, with peaks corresponding to Se_T^{-1} (Se $3d_{5/2}$; 53.8 eV) and Se_B^0 (Se $3d_{3/2}$; 55.1 eV) shifting to lower binding energy values compared with the uncycled sample (Fig. 3b; 54.9 eV for Se $3d_{5/2}$ (terminal Se; Se_T^{-1}) and 55.8 eV for Se $3d_{3/2}$ (bridging Se; Se_B^0)), demonstrating the changes in the Se environment owing to the strong chemical interactions between Mo_2C and NaPSes. Furthermore, the presence of Na 1*s* and Cl 2*p* in the survey spectrum indicated the decomposition of the electrolyte. More precisely, the deconvoluted Na 1*s* (Fig. S16c) exhibited three fitted peaks at 1070.4, 1070.8, and 1071.7 eV, corresponding to the carboxymethylcellulose–Na (–COO–Na–), solid-state CEI–Na, and –Se–Na– bonds, respectively [71]. Similarly, the deconvoluted Cl 2*p* (Fig. S16d) displayed two well-fitted peaks at 284.6 and 288.8 eV, which are attributed to the decomposition of the electrolyte or perchlorate salt [79]. The FE–SEM micrograph of the cycled Se@P–N–C@Mo_2C cathode (Fig. S16e) revealed that the fibrous morphology remained intact; however, the surface was covered with plate-like side products primarily composed of NaPSe deposits. A digital photograph of the cycled glass fiber (GF) in the inset revealed a slightly yellowish color, indicating the restricted diffusion of PSes. Conversely, the FE–SEM image of the Se@P–N–C cathode (Fig. S16f) confirmed the deposition of a thick layer of the reaction products. This observation was also validated by the dark brown color of cycled GF in the inset. Besides, a concomitant change in the color of base electrolyte solution [EC:DEC (1:1)] for Se@P–N–C@Mo_2C and Se@P–N–C cycled electrodes (Fig. S17) also indicate better inhibition of PSe in the case of former. Therefore, from the above results, it can be concluded that the Se@P–N–C@Mo_2C cathode not only maintains its structural integrity after prolonged cycling but also slows down the migration of PSes toward the cathode, thus increasing the effective active-material utilization and improving electrochemical performance. Overall, the post-cycling characterization results indicated that the presence of the Mo_2C catalyst effectively inhibited PSe diffusion, accelerated their electrocatalytic conversion, and promoted kinetically favored redox kinetics.

3.6. Full cell assembly and electrochemical details for sodium/potassium-ion storage

Furthermore, as proof of concept, we designed Na-ion full cells employing Se@P–N–C@Mo_2C as the anode and spray-drying-derived high-voltage spherical-type $Na_3V_2(PO_4)_3$/C (NVP/C) as the cathode. Fig. 7a–f shows the morphological features of the NVP/C cathode alongside half- and full cell electrochemical outcomes. The FE-SEM micrograph (Fig. 7a) of the as-prepared NVP/C cathode revealed the formation of non-agglomerated 3D microspheres with an average diameter of ~1.8 μm. Furthermore, the high-magnification FE–SEM image (inset of Fig. 7a) highlighted numerous pores across the entire surface of the microspheres, which were formed by the decomposition of various carbonate or ammonium species into gaseous products during heat treatment. The XRD pattern (Fig. 7b) displayed sharp and distinct peaks indexed to the NVP phase (*Hexagonal* crystal, $R\bar{3}c$ space group). The wide hump at $2\theta = 22.9^{\circ}$ was attributed to the dextrin-derived carbonaceous species. The assembled half-cell underwent a rate-capability test at various C-rates (Fig. S18a and Fig. 7c). The cell exhibited typical voltage profiles (Fig. S18a) with a flat discharge voltage plateau at ~3.35 V for low C-rates, shifting to lower voltages for high C-rates owing to the polarization effect. The cell delivered initial discharge capacities of 90, 90, 88, 82, 75, 66, 56, 50, and 33 mA h g^{-1} at C-rates of 0.05, 0.1, 0.2, 0.3, 0.5, 0.7, 1.0, 2.0, and 3.0C, respectively. Moreover, when cycled at 0.5C-rate (Fig. 7d), the cell displayed a capacity retention of ~69 % after 100 continuous charge–discharge processes. Subsequently, an NVP/C//Se@P–N–C@Mo_2C full cell was assembled by combining 6.75 and 0.90 mg cm^{-2} NVP/C and Se@P–N–C@Mo_2C as the cathode and anode, respectively, in a standard coin cell. Fig. 7e illustrates the schematic of the full Na-ion battery comprising the NVP/C//Se@P–N–C@Mo_2C pair. The voltage profiles (Fig. S18b) revealed that the cell exhibited a charge–discharge capacity of 146/88 mA h g^{-1} at 0.1C in the voltage range of 0.5–3.8 V. When cycled at a C-rate of 0.1C (Fig. 7f), the full cell displayed a capacity retention of ~70 % after the 60th cycle, emphasizing the large-scale energy-storage capability of the full cell.

Similarly, we engineered K-ion full-cells employing Se@P–N–C@-Mo_2C as the anode and P3-type $K_{0.5}Mn_{0.8}Co_{0.1}Ni_{0.1}O_2$ (KMCNO) microcuboids derived *via* ethanol-mediated co-precipitation as the high-voltage cathode. Fig. 7g–l outlines the morphological features of the KMCNO cathode along with the electrochemical outcomes of the half- and full cells. The FE-SEM micrographs (Fig. 7g and inset) revealed a distinctive cuboid-type morphology. The XRD pattern (Fig. 7h) displayed sharp, distinct peaks indexed to the P3-structure KMCNO phase, which is characterized by a *hexagonal* crystal and *R3m* space group. The assembled half-cell was subjected to a rate-capability test at various current densities (Fig. S19a and Fig. 7i). The cell delivered discharge capacities of 66, 54, 26, and 7 mA h g^{-1} at current densities of 10, 20, 50, and 100 mA g^{-1}, respectively. Moreover, when cycled at 20 mA g^{-1}, the cell displayed a capacity retention of ~51 % after 100 continuous charge–discharge processes (Fig. 7j). Consequently, a KMCNO// Se@P–N–C@Mo_2C full cell was constructed by combining KMCNO (6.48 mg cm^{-2}) and Se@P–N–C@Mo_2C (0.73 mg cm^{-2}) as the cathode and anode, respectively (Fig. 7k). The voltage profiles (Fig. S19b) revealed that the cell exhibited a charge–discharge capacity of 28/33 mA h g^{-1} at 20 mA g^{-1} in the voltage range of 0.5–3.7 V. When cycled at

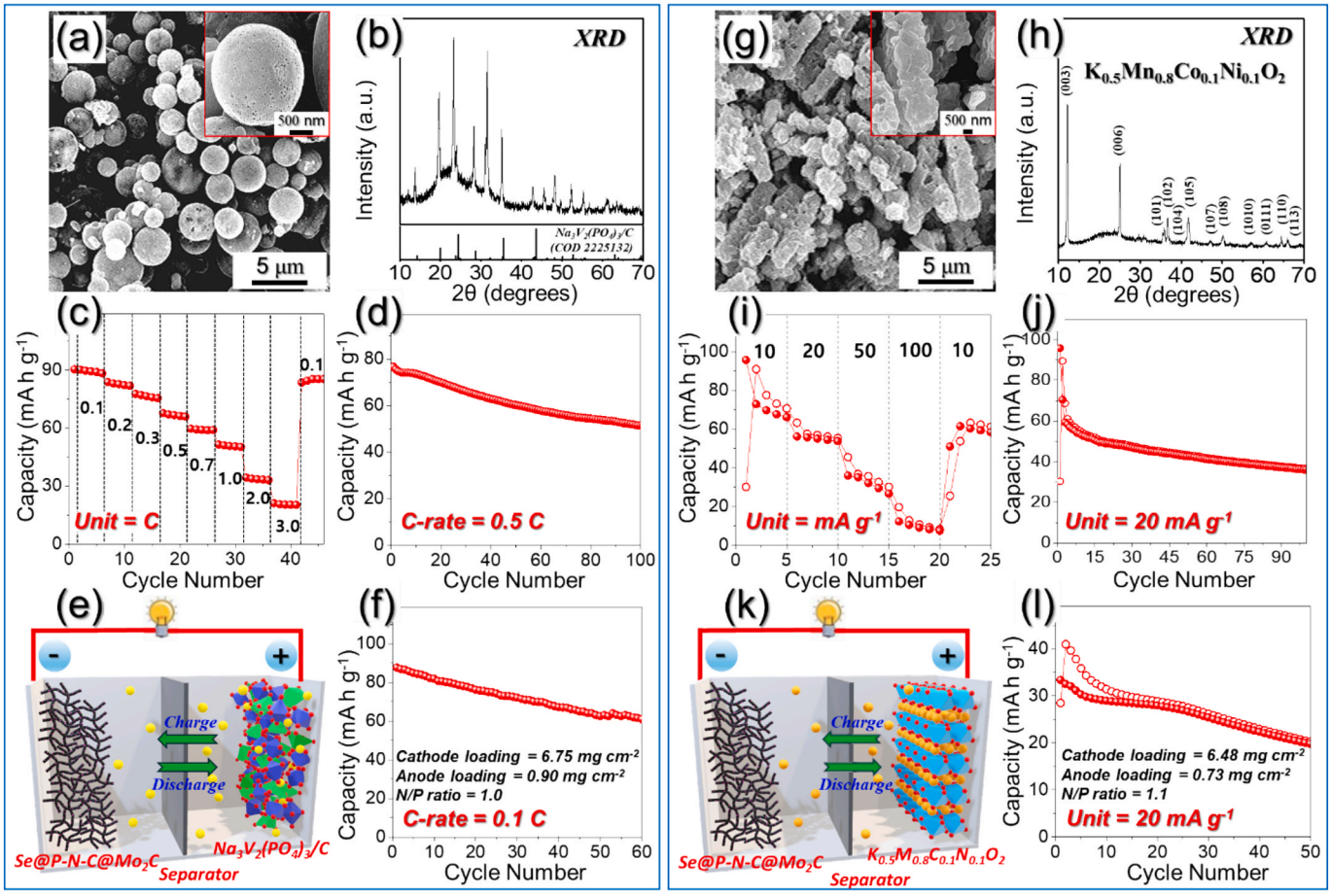

Fig. 7. Morphological and half/full-cell electrochemical studies using (a–f) $Na_3V_2(PO_4)_3$/C (NVP/C) and (g–l) $K_{0.5}Mn_{0.8}Co_{0.1}Ni_{0.1}O_2$ (KMCNO) cathodes: (a, g) FE–SEM micrographs, (b, h) XRD patterns, (c, i) Rate capability tests, (d, j) Cycling performance of cathodic half-cell (e, k) Schematic representation of full cells, and (f, i) Cycling performance of the full cells.

20 mA g^{-1} (Fig. 7l), the full cell displayed capacity retention of ~59 % after the 50th cycle, underscoring the extensive energy-storage capability. It is crucial to emphasize that we synthesized the cathode materials ourselves, necessitating further refinement to achieve optimal cycling performance for the half- and full cells.

Overall, we have demonstrated the synthesis and applicability of an N-doped porous and conductive framework comprising ultrafine Mo_2C catalysts as a suitable host for Se infiltration. This framework realized considerable electrochemical performance in half- and full cell configurations for Na/K-ion storage.

4. Conclusions

In summary, we synthesized a highly porous and conductive N-doped carbonaceous framework comprising well-embedded ultrafine Mo_2C catalysts (P–N–C@Mo_2C). This framework acted as an effective host for Se infiltration (Se@P–N–C@Mo_2C). The thermal decomposition of the elongated PS phase yielded 1D continuous porous tunnel-like channels, which guaranteed facile electrolyte percolation, the smooth and rapid diffusion of electrons/ions *via* the decreased diffusion length, and the accommodation of undesirable volume perturbations. Additionally, the N-doping within the carbon species enhanced the electronic conductivity of the nanostructure. The presence of the Mo_2C catalyst facilitated the efficient trapping and electrocatalytic conversion of NaPSe species *via* the electrophilic coupling interactions between $Mo^{\delta+}$ and Se_x^{2-} in the Mo_2C and Na_2Se_x species, respectively, resulting in enhanced active-material utilization. Thus, the cell featuring the Se@P–N–C@Mo_2C cathode exhibited remarkable high-rate capability (up to 10.0C) and stable cycling performance at low (0.5C) and high (1.0C) C-rates. Similarly, when deployed for K-ion storage, the Se@P–N–C@Mo_2C cathode maintained a high and stable discharge capacity, 235 mA h g^{-1} (87 % retention, 220 cycles) at a C-rate of 1.0C. Even in a full cell configuration, the electrode demonstrated the reversible intercalation/deintercalation of Na/K ions, underscoring its suitability for commercial applications. Therefore, we posit that the physical and electrochemical advancements presented in this paper will significantly enhance our current understanding of alkali metal–Se batteries.

CRediT authorship contribution statement

Sung Woo Cho: Writing – original draft, Visualization, Software, Investigation, Conceptualization. **Hyun Ho Choi:** Visualization, Software, Investigation, Formal analysis, Conceptualization. **Thillai Govindaraja Senthamaraikannan:** Writing – original draft, Methodology, Data curation. **Dong–Hee Lim:** Writing – original draft, Visualization, Methodology, Investigation. **Gi Dae Park:** Visualization, Software, Methodology. **Chungyeon Cho:** Visualization, Validation, Software. **Sang Mun Jeong:** Writing – original draft, Investigation. **Rakesh Saroha:** Writing – review & editing, Writing – original draft, Visualization, Supervision, Investigation, Conceptualization. **Jung Sang Cho:** Writing – review & editing, Writing – original draft, Supervision, Project administration, Funding acquisition, Conceptualization.

Declaration of competing interest

The authors declare that they have no known competing financial interests or personal relationships that could have appeared to influence the work reported in this paper.

Acknowledgments

This work was supported by the National Research Foundation of Korea (NRF) grant funded by the Korea government (MSIT) (Grant No.: RS-2023-00217581, RS-2025-00556955).

Appendix A. Supplementary data

Supplementary data to this article can be found online at https://doi.org/10.1016/j.cej.2025.162456.

Data availability

No data was used for the research described in the article.

References

[1] Z. Wang, B. Wang, Y. Yang, Y. Cui, Z. Wang, B. Chen, G. Qian, Mixed-metal–organic framework with effective lewis acidic sites for sulfur confinement in high-performance lithium–sulfur batteries, ACS Appl. Mater. Interfaces 7 (2015) 20999–21004, https://doi.org/10.1021/acsami.5b07024.
[2] R. Saroha, H.S. Ka, G.D. Park, C. Cho, D.-W. Kang, J.S. Cho, Long-term stability of lithium–sulfur batteries via synergistic integration of nitrogen-doped graphitic carbon-coated cobalt selenide nanocrystals within porous three-dimensional graphene-carbon nanotube microspheres, J. Power Sources 592 (2024) 233893, https://doi.org/10.1016/j.jpowsour.2023.233893.
[3] R. Saroha, J.-H. Ahn, J.S. Cho, A short review on dissolved lithium polysulfide catholytes for advanced lithium-sulfur batteries, Korean J. Chem. Eng. 38 (2021) 461–474, https://doi.org/10.1007/s11814-020-0729-5.
[4] S. Soni, R. Kumar, A. Sodhiya, S. Patel, A.K. Singh, Trapping lithium polysulfides within the cathode by doping MnO_2 nanorods into an exfoliated graphite/sulfur composite for lithium–sulfur batteries, Carbon Lett. 32 (2022) 1425–1432, https://doi.org/10.1007/s42823-022-00390-2.
[5] A. Manthiram, Y. Fu, Y.-S. Su, Challenges and prospects of lithium–sulfur batteries, Acc. Chem. Res. 46 (2013) 1125–1134, https://doi.org/10.1021/ar300179v.
[6] C. Deng, Z. Wang, S. Wang, J. Yu, D.J. Martin, A.K. Nanjundan, Y. Yamauchi, Double-layered modified separators as shuttle suppressing interlayers for lithium–sulfur batteries, ACS Appl. Mater. Interfaces 11 (2018) 541–549, https://doi.org/10.1021/acsami.8b14196.
[7] D. Son, W.-G. Lim, J. Lee, A short review of the recent developments in functional separators for lithium-sulfur batteries, Korean J. Chem. Eng. 40 (2023) 473–487, https://doi.org/10.1007/s11814-022-1372-0.
[8] E. Karaseva, L. Khramtsova, N. Shakirova, E. Kuzmina, V. Kolosnitsyn, Sulfur solubility in sulfolane electrolytes sutable for lithium-sulfur batteries, Russ. J. Gen. Chem. 93 (2023) 1155–1161, https://doi.org/10.1134/S107036322305016X.
[9] Y. Sun, J. Liao, J. Sun, L. Duan, Y. Du, J. Bao, X. Zhou, Zn-MOF-74-derived carbon nanorods as an efficient Se host for K-Se batteries, ACS Appl. Energy Mater. 5 (2022) 13023–13030, https://doi.org/10.1021/acsaem.2c02679.
[10] R. Saroha, J. Heo, X. Li, N. Angulakshmi, Y. Lee, H.-J. Ahn, J.-H. Ahn, J.-H. Kim, Asymmetric separator integrated with ferroelectric-$BaTiO_3$ and mesoporous-CNT for the reutilization of soluble polysulfide in lithium-sulfur batteries, J. Alloys Compd. 893 (2022) 162272, https://doi.org/10.1016/j.jallcom.2021.162272.
[11] R. Saroha, J. Heo, Y. Liu, N. Angulakshmi, Y. Lee, K.-K. Cho, H.-J. Ahn, J.-H. Ahn, V_2O_3-decorated carbon nanofibers as a robust interlayer for long-lived, high-performance, room-temperature sodium–sulfur batteries, Chem. Eng. J. 431 (2022) 134205, https://doi.org/10.1016/j.cej.2021.134205.
[12] C.S. Kim, R. Saroha, H.H. Choi, J.H. Oh, G.D. Park, D.-W. Kang, J.S. Cho, High-performance cathode promoted by reduced graphene oxide nanofibers with well-defined interconnected meso-/micro pores for rechargeable Li-Se batteries, J. Ind. Eng. Chem. 121 (2023) 489–498, https://doi.org/10.1016/j.jiec.2023.02.004.
[13] Y. Liu, L. Si, X. Zhou, X. Liu, Y. Xu, J. Bao, Z. Dai, A selenium-confined microporous carbon cathode for ultrastable lithium–selenium batteries, J. Mater. Chem. A 2 (2014) 17735–17739, https://doi.org/10.1039/C4TA03141E.
[14] K. Han, Z. Liu, J. Shen, Y. Lin, F. Dai, H. Ye, A free-standing and ultralong-life lithium-selenium battery cathode enabled by 3D mesoporous carbon/graphene hierarchical architecture, Adv. Funct. Mater. 25 (2015) 455–463, https://doi.org/10.1002/adfm.201402815.
[15] Y.J. Hong, Y.C. Kang, Selenium-impregnated hollow carbon microspheres as efficient cathode materials for lithium-selenium batteries, Carbon 111 (2017) 198–206, https://doi.org/10.1016/j.carbon.2016.09.069.
[16] S. Jiang, Z. Zhang, Y. Lai, Y. Qu, X. Wang, J. Li, Selenium encapsulated into 3D interconnected hierarchical porous carbon aerogels for lithium–selenium batteries with high rate performance and cycling stability, J. Power Sources 267 (2014) 394–404, https://doi.org/10.1016/j.jpowsour.2014.05.116.
[17] Z. Yi, L. Yuan, D. Sun, Z. Li, C. Wu, W. Yang, Y. Wen, B. Shan, Y. Huang, High-performance lithium–selenium batteries promoted by heteroatom-doped microporous carbon, J. Mater. Chem. A 3 (2015) 3059–3065, https://doi.org/10.1039/C4TA06141A.
[18] T. Liu, M. Jia, Y. Zhang, J. Han, Y. Li, S. Bao, D. Liu, J. Jiang, M. Xu, Confined selenium within metal-organic frameworks derived porous carbon microcubes as cathode for rechargeable lithium–selenium batteries, J. Power Sources 341 (2017) 53–59, https://doi.org/10.1016/j.jpowsour.2016.11.099.
[19] L. Cheng, C. Ma, W. Lu, X. Wang, H. Yue, D. Zhang, Z. Xing, A graphitized hierarchical porous carbon as an advanced cathode host for alkali metal-selenium batteries, Chem. Eng. J. 433 (2022) 133527, https://doi.org/10.1016/j.cej.2021.133527.
[20] R. Saroha, T.S. Khan, M. Chandra, R. Shukla, A.K. Panwar, A. Gupta, M.A. Haider, S. Basu, R.S. Dhaka, Electrochemical properties of $Na_{0.66}V_4O_{10}$ nanostructures as

cathode material in rechargeable batteries for energy storage applications, ACS Omega 4 (2019) 9878–9888, https://doi.org/10.1021/acsomega.9b00105.
[21] X. Yang, S. Wang, H. Li, J. Tseng, Z. Wu, S. Indris, H. Ehrenberg, X. Guo, W. Hua, Unveiling the correlation between structural alterations and enhanced high-voltage cyclability in Na-deficient P3-type layered cathode materials via Li incorporation, Electron 2 (2024) e18.
[22] L. Sun, J. Zeng, X. Wan, C. Peng, J. Wang, C. Lin, M. Zhu, J. Liu, Recent progress of interface modification of layered oxide cathode material for sodium-ion batteries, Electron 2 (2024) e31.
[23] H. Ou, B. Pei, Y. Zhou, M. Yang, J. Pan, S. Liang, X. Cao, From natural fibers to high-performance anodes: sisal hemp derived hard carbon for Na-/K-ion batteries and mechanism exploration, Small Methods 9 (2025) 2400839, https://doi.org/10.1002/smtd.202400839.
[24] P. Hu, F. Xiao, H. Wang, A.L. Rogach, Dual-functional hosts derived from metal-organic frameworks reduce dissolution of polyselenides and inhibit dendrite growth in a sodium-selenium battery, Adv. Energy Mater. 51 (2022) 249–258, https://doi.org/10.1016/j.ensm.2022.06.019.
[25] H. Wang, Y. Jiang, A. Manthiram, Long cycle life, low self-discharge sodium–selenium batteries with high selenium loading and suppressed polyselenide shuttling, Adv. Energy Mater. 8 (2018) 1701953, https://doi.org/10.1002/aenm.201701953.
[26] J. Ding, H. Zhou, H. Zhang, T. Stephenson, Z. Li, D. Karpuzov, D. Mitlin, Exceptional energy and new insight with a sodium–selenium battery based on a carbon nanosheet cathode and a pseudographite anode, Energy Environ. Sci. 10 (2017) 153–165, https://doi.org/10.1039/C6EE02274J.
[27] F. Zhang, P. Xiong, X. Guo, J. Zhang, W. Yang, W. Wu, H. Liu, G. Wang, A nitrogen, sulphur dual-doped hierarchical porous carbon with interconnected conductive polyaniline coating for high-performance sodium-selenium batteries, Energy Storage Mater. 19 (2019) 251–260, https://doi.org/10.1016/j.ensm.2019.03.019.
[28] S. Li, H. Yang, R. Xu, Y. Jiang, Y. Gong, L. Gu, Y. Yu, Selenium embedded in MOF-derived N-doped microporous carbon polyhedrons as a high performance cathode for sodium–selenium batteries, Mater. Chem. Front. 2 (2018) 1574–1582, https://doi.org/10.1039/C8QM00177D.
[29] Y. Deng, L. Gong, Y. Pan, X. Cheng, H. Zhang, A long life sodium–selenium cathode by encapsulating selenium into N-doped interconnected carbon aerogels, Nanoscale 11 (2019) 11671–11678, https://doi.org/10.1039/C9NR00701F.
[30] W.-D. Dong, Y. Li, C.-F. Li, Z.-Y. Hu, L.-C. Hsu, L.-H. Chen, Y. Li, A. Lei, B.-L. Su, Atomically dispersed Co-N_4C_2 catalytic sites for wide-temperature Na-Se batteries, Nano Energy 105 (2023) 108005, https://doi.org/10.1016/j.nanoen.2022.108005.
[31] W.-D. Dong, C.-Y. Wang, C.-F. Li, F.-J. Xia, W.-B. Yu, L. Wu, H. Mohamed, Z.-Y. Hu, J. Liu, L.-H. Chen, The free-standing N-doped Murray carbon framework with the engineered quasi-optimal Se/C interface for high–Se-loading Li/Na–Se batteries at elevated temperature, Mater. Today Energy 21 (2021) 100808, https://doi.org/10.1016/j.mtener.2021.100808.
[32] W. Dong, H. Chen, F. Xia, W. Yu, J. Song, S. Wu, Z. Deng, Z.-Y. Hu, T. Hasan, Y. Li, Selenium clusters in Zn-glutamate MOF derived nitrogen-doped hierarchically radial-structured microporous carbon for advanced rechargeable Na–Se batteries, J. Mater. Chem. A 6 (45) (2018) 22790–22797, https://doi.org/10.1039/C8TA07662F.
[33] Y.J. Hong, K.C. Roh, Y.C. Kang, Mesoporous graphitic carbon microspheres with a controlled amount of amorphous carbon as an efficient Se host material for Li–Se batteries, J. Mater. Chem. A 6 (2018) 4152–4160, https://doi.org/10.1039/C7TA11112F.
[34] Z. Erdol, A. Ata, R. Demir-Cakan, Sodium-selenium batteries with outstanding rate capability by introducing cubic Mn_2O_3 electrocatalyst, ChemSusChem 17 (2024) e202300998, https://doi.org/10.1002/cssc.202300998.
[35] H. Wang, Y. Jiang, A. Manthiram, N-doped Fe_3C@C as an efficient polyselenide reservoir for high-performance sodium-selenium batteries, Energy Storage Mater. 16 (2019) 374–382, https://doi.org/10.1016/j.ensm 2018.06.014.
[36] R. Shi, N. Chen, B. Li, L. Zhang, T. Gao, W. Lian, Z. Wang, H. Cui, W. Song, Design of β-Mo_2C with an appropriate intercalation potential as an anode material toward lithium ion batteries, Solid State Ion. 405 (2024) 116438, https://doi.org/10.1016/j.ssi.2023.116438.
[37] M. Chen, C. Song, C. Liang, B. Zhang, Y. Sun, S. Li, L. Lin, P. Xu, Crystalline phase induced Raman enhancement on molybdenum carbides, Inorg. Chem. Front. 9 (2022) 2575–2582, https://doi.org/10.1039/D2QI00543C.
[38] R. Saroha, J.H. Oh, J.S. Lee, Y.C. Kang, S.M. Jeong, D.-W. Kang, C. Cho, J.S. Cho, Hierarchically porous nanofibers comprising multiple core–shell Co_3O_4@graphitic carbon nanoparticles grafted within N-doped CNTs as functional interlayers for excellent Li–S batteries, Chem. Eng. J. 426 (2021) 130805, https://doi.org/10.1016/j.cej.2021.130805.
[39] L. Duan, Y. Xu, Z. Zhang, J. Xu, J. Liao, J. Xu, Y. Sun, Y. He, X. Zhou, A high-performance cathode for potassium-ion batteries based on uniform P3-type $K_{0.5}Mn_{0.8}Co_{0.1}Ni_{0.1}O_2$ porous microcuboids, J. Mater. Chem. A 9 (2021) 22820–22826, https://doi.org/10.1039/D1TA07108D.
[40] G. Kresse, J. Furthmüller, Efficient iterative schemes for ab initio total-energy calculations using a plane-wave basis set, Phys. Rev. B 54 (1996) 11169, https://doi.org/10.1103/PhysRevB.54.11169.
[41] G. Kresse, J. Hafner, Ab initio molecular-dynamics simulation of the liquid-metal-amorphous-semiconductor transition in germanium, Phys. Rev. B 49 (1994) 14251–14269, https://doi.org/10.1103/PhysRevB.49.14251.
[42] G. Kresse, J. Hafner, Ab initio molecular dynamics for liquid metals, Phys. Rev. B 47 (1993) 558, https://doi.org/10.1103/PhysRevB.47.558.
[43] G. Kresse, J. Furthmüller, Efficiency of ab-initio total energy calculations for metals and semiconductors using a plane-wave basis set, Comput. Mater. Sci. 6 (1996) 15–50, https://doi.org/10.1016/0927-0256(96)00008-0.
[44] P.E. Blöchl, Projector augmented-wave method, Phys. Rev. B 50 (1994) 17953–17979, https://doi.org/10.1103/PhysRevB.50.17953.
[45] G. Kresse, D. Joubert, From ultrasoft pseudopotentials to the projector augmented-wave method, Phys. Rev. B 59 (1999) 1758–1775, https://doi.org/10.1103/PhysRevB.59.1758.
[46] J.P. Perdew, K. Burke, M. Ernzerhof, Generalized gradient approximation made simple, Phys. Rev. Lett. 77 (1996) 3865, https://doi.org/10.1103/PhysRevLett.77.3865.
[47] H.J. Monkhorst, J.D. Pack, Special points for Brillouin-zone integrations, Phys. Rev. B 13 (1976) 5188–5192, https://doi.org/10.1103/PhysRevB.13.5188.
[48] R. Saroha, J.H. Oh, Y.H. Seon, Y.C. Kang, J.S. Lee, J.S. Cho, Freestanding interlayers for Li-S batteries: design and synthesis of hierarchically porous N-doped C nanofibers comprising vanadium nitride quantum dots and MOF-derived hollow N-doped C nanocages, J. Mater. Chem. A 9 (2021) 11651–11664, https://doi.org/10.1039/D1TA01802G.
[49] Y. Lei, Y. Yang, Y. Liu, Y. Zhu, M. Jia, Y. Zhang, K. Zhang, A. Yu, J. Liu, J. Zhai, Nitrogen-doped porous carbon nanosheets strongly coupled with Mo_2C nanoparticles for efficient electrocatalytic hydrogen evolution, Nanoscale Res. Lett. 14 (2019) 329, https://doi.org/10.1186/s11671-019-3147-z.
[50] D. Wang, J. Wang, X. Luo, Z. Wu, L. Ye, In situ preparation of Mo_2C nanoparticles embedded in ketjenblack carbon as highly efficient electrocatalysts for hydrogen evolution, ACS Sustain. Chem. Eng. 6 (2018) 983–990, https://doi.org/10.1021/acssuschemeng.7b03317.
[51] G. Li, J. Yu, Z. Zhou, R. Li, Z. Xiang, Q. Cao, L. Zhao, X. Wang, X. Peng, H. Liu, N-doped Mo_2C nanobelts/graphene nanosheets bonded with hydroxy nanocellulose as flexible and editable electrode for hydrogen evolution reaction, Iscience 19 (2019) 1090–1100, https://doi.org/10.1016/j.isci.2019.08.055.
[52] J.S. Lee, J.-S. Park, K.W. Baek, R. Saroha, S.H. Yang, Y.C. Kang, J.S. Cho, Coral-like porous microspheres comprising polydopamine-derived N-doped C-coated $MoSe_2$ nanosheets composited with graphitic carbon as anodes for high-rate sodium-and potassium-ion batteries, Chem. Eng. J. 456 (2022) 141118, https://doi.org/10.1016/j.cej.2022.141118.
[53] R. Saroha, H.H. Choi, J.S. Cho, Boosting redox kinetics using rationally engineered cathodic interlayers comprising porous rGO–CNT framework microspheres with $NiSe_2$-core@N-doped graphitic carbon shell nanocrystals for stable Li–S batteries, Chem. Eng. J. 473 (2023) 145391, https://doi.org/10.1016/j.cej.2023.145391.
[54] G.D. Park, J.S. Cho, J.-K. Lee, Y.C. Kang, Na-ion storage performances of $FeSe_x$ and Fe_2O_3 hollow nanoparticles-decorated reduced graphene oxide balls prepared by nanoscale Kirkendall diffusion process, Sci. Rep. 6 (2016) (2016) 22432, https://doi.org/10.1038/srep22432.
[55] J.S. Lee, M.S. Jo, R. Saroha, D.S. Jung, Y.H. Seon, J.S. Lee, Y.C. Kang, D.W. Kang, J. S. Cho, Hierarchically well-developed porous graphene nanofibers comprising N-doped graphitic C-coated cobalt oxide hollow nanospheres as anodes for high-rate Li-ion batteries, Small 16 (2020) 2002213.
[56] J.S. Lee, R. Saroha, S.H. Oh, D.H. Shin, S.M. Jeong, J.K. Kim, J.S. Cho, Rational design of perforated bimetallic (Ni, Mo) sulfides/N-doped graphitic carbon composite microspheres as anode materials for superior Na-ion batteries, Small Methods 5 (2021) 2100195, https://doi.org/10.1002/smll.202002213.
[57] C.S. Kim, J.S. Lee, R. Saroha, Y.B. Park, Y. Chan Kang, D.-W. Kang, S.M. Jeong, J. S. Cho, Porous nitrogen-doped graphene nanofibers comprising metal organic framework-derived hollow and ultrafine layered double metal oxide nanocrystals as high-performance anodes for lithium-ion batteries, J. Power Sources 523 (2022) 231030, https://doi.org/10.1016/j.jpowsour.2022.231030.
[58] J.S. Lee, R. Saroha, J.H. Oh, C. Cho, B. Jin, D.-W. Kang, J.S. Cho, Camphene-derived hollow and porous nanofibers decorated with hollow NiO nanospheres and graphitic carbon as anodes for efficient lithium-ion storage, J. Ind. Eng. Chem. 114 (2022) 276–287, https://doi.org/10.1016/j.jiec.2022.07.017.
[59] R. Saroha, J.S. Cho, Nanofibers comprising interconnected chain-like hollow N-doped C nanocages as 3D free-standing cathodes for Li–S batteries with super-high sulfur content and lean electrolyte/sulfur ratio, Small Methods 6 (2022) 2200049, https://doi.org/10.1002/smtd.202200049.
[60] J.S. Lee, R. Saroha, J.S. Cho, Porous microspheres comprising $CoSe_2$ nanorods coated with N-doped graphitic C and polydopamine-derived C as anodes for long-lived Na-ion batteries, Nano-Micro Lett. 14 (2022) 1–22, https://doi.org/10.1007/s40820-022-00855-z.
[61] C.S. Kim, R. Saroha, J.S. Cho, N-Doped graphene nanofibers with porous channel comprising FeS nanocrystals and intertwined N-doped CNTs as efficient interlayers for Li-S batteries, Int. J. Energy Res. 121 (2023) 489–498, https://doi.org/10.1155/2023/3610577.
[62] Y.H. Seon, R. Saroha, J.S. Cho, Hierarchically porous N-doped C nanofibers comprising TiO_2 quantum dots and ZIF-8-derived hollow C nanocages as ultralight interlayer for stable Li–S batteries, Compos. B Eng. 237 (2022) 109856, https://doi.org/10.1016/j.compositesb.2022.109856.
[63] R. Saroha, Y.H. Seon, B. Jin, Y.C. Kang, D.-W. Kang, S.M. Jeong, J.S. Cho, Self-supported hierarchically porous 3D carbon nanofiber network comprising Ni/Co/$NiCo_2O_4$ nanocrystals and hollow N-doped C nanocages as sulfur host for highly reversible Li–S batteries, Chem. Eng. J. 446 (2022) 137141, https://doi.org/10.1016/j.cej.2022.137141.
[64] S.H. Yang, J.M. Choi, R. Saroha, S.W. Cho, Y.C. Kang, J.S. Cho, Hollow porous carbon nanospheres containing polar cobalt sulfide (Co_9S_8) nanocrystals as electrocatalytic interlayers for the reutilization of polysulfide in lithium–sulfur batteries, J. Colloid Interface Sci. 645 (2023) 33–44, https://doi.org/10.1016/j.jcis.2023.04.083.

[65] D. Ruan, R. Lin, K. Jiang, X. Yu, Y. Zhu, Y. Fu, Z. Wang, H. Yan, W. Mai, High-performance porous molybdenum oxynitride based fiber supercapacitors, ACS Appl. Mater. Interfaces 9 (2017) 29699–29706, https://doi.org/10.1021/acsami.7b07522.
[66] C.D. Wagner, NIST X-ray photoelectron spectroscopy database, NIST Standarad Reference Database 20 (2000).
[67] J. Chastain, R.C. King Jr, Handbook of X-ray photoelectron spectroscopy, Perkin-Elmer Corporation 40 (1992) 221.
[68] R. Saroha, H.S. Ka, J.S. Cho, A novel three-dimensional ordered mesoporous microspheres comprising N-doped graphitic carbon-coated Fe_xP nanoparticles as multifunctional interlayers to suppress polysulfide crossover in Li–S batteries, Appl. Surf. Sci. 612 (2022) 155892, https://doi.org/10.1016/j.apsusc.2022.155892.
[69] J.M. Choi, R. Saroha, J.S. Kim, M.R. Jang, J.S. Cho, Porous nanofibers comprising VN nanodots and densified N-doped CNTs as redox-active interlayers for Li–S batteries, J. Power Sources 559 (2023) 232632, https://doi.org/10.1016/j.jpowsour.2023.232632.
[70] J.S. Lee, H.S. Ka, R. Saroha, Y.C. Kang, D.-W. Kang, J.S. Cho, Three-dimensional hierarchically porous micro sponge-ball comprising anatase TiO_2 nanodots and nitrogen-doped graphitic carbon as anodes for ultra-stable lithium-ion batteries, J. Energy Storage 66 (2023) 107396, https://doi.org/10.1016/j.est.2023.107396.
[71] D. Zhao, L. Wang, M. Qiu, N. Zhang, Amorphous Se restrained by biomass-derived defective carbon for stable Na–Se batteries, ACS Appl. Energy Mater. 4 (2021) 7219–7225, https://doi.org/10.1021/acsaem.1c01317.
[72] R. Saroha, A.K. Panwar, Effect of in situ pyrolysis of acetylene (C_2H_2) gas as a carbon source on the electrochemical performance of $LiFePO_4$ for rechargeable lithium-ion batteries, J. Phys. D: Appl. Phys. 50 (2017) 255501, https://doi.org/10.1088/1361-6463/aa708c.
[73] S.-K. Park, J.-S. Park, Y.C. Kang, Selenium-infiltrated metal–organic framework-derived porous carbon nanofibers comprising interconnected bimodal pores for Li–Se batteries with high capacity and rate performance, J. Mater. Chem. A 6 (2018) 1028–1036, https://doi.org/10.1039/C7TA09676C.
[74] R. Wang, D. Wang, Y. Dong, B. Xie, X. Wu, Q. Wu, S. Zhu, G. Diao, M. Chen, Recent progress of advanced carbon-based cathode in sodium-selenium batteries, J. Alloys Compd. 952 (2023) 169980, https://doi.org/10.1016/j.jallcom.2023.169980.
[75] J. Ding, Y. Wang, Z. Huang, W. Song, C. Zhong, J. Ding, W. Hu, Toward theoretical capacity and superhigh power density for potassium–selenium batteries via facilitating reversible potassiation kinetics, ACS Appl. Mater. Interfaces 14 (2022) 6828–6840, https://doi.org/10.1021/acsami.1c22623.
[76] R.F. Bader, A quantum theory of molecular structure and its applications, Chem. Rev. 91 (1991) 893–928, https://doi.org/10.1021/cr00005a013.
[77] Y.-S. Han, C.-M. Lee, C.-M. Chon, J.A. Kwon, J.-H. Park, Y.-J. Shin, D.-H. Lim, Enhanced oxidation resistance of $NaBH_4$-treated mackinawite (FeS): Application to Cr (VI) and As (III) removal, Chem. Eng. J. 353 (2018) 890–899, https://doi.org/10.1016/j.cej.2018.07.132.
[78] D.Y. Shin, Y.-J. Shin, M.-S. Kim, J.A. Kwon, D.-H. Lim, Density functional theory–based design of a Pt-skinned PtNi catalyst for the oxygen reduction reaction in fuel cells, Appl. Surf. Sci. 565 (2021) 150518, https://doi.org/10.1016/j.apsusc.2021.150518.
[79] S. Wang, C. Li, X. Fan, S. Wen, H. Lu, H. Dong, J. Wang, Y. Quan, S. Li, Selection of sodium salt electrolyte compatible with $Na_{0.67}Ni_{0.15}Fe_{0.2}Mn_{0.65}O_2$ cathode for sodium-ion batteries, Energy Technol. 9 (2021) 2100190, https://doi.org/10.1002/ente.202100190.